The thesis committee for Guneet Kaur
Certifies that this is the approved version of the following thesis:

Numerical Errors and Accuracy-Efficiency Tradeoff in Frequency and Time-Domain Integral Equation Solvers

APPROVED BY

SUPERVISING COMMITTEE:

Supervisor:

A. E. Yilmaz

Hao Ling

Numerical Errors and Accuracy-Efficiency Tradeoff in Frequency and Time-Domain Integral Equation Solvers

by

Guneet Kaur, B. S. E.

Thesis

Presented to the Faculty of the Graduate School of

The University of Texas at Austin

in Partial Fulfillment

of the Requirements

for the Degree of

Master of Science in Engineering

The University of Texas at Austin

December 2010

Dedication

To my parents

Acknowledgements

I would like to acknowledge the invaluable guidance and immense patience of my research advisor Professor Ali E. Yilmaz and would like to thank him for his assistance and direction, without which this thesis would not have been possible. I am grateful to him for being always available for his help and support.

I would also like to thank Professor Hao Ling for his helpful comments and suggestions.

I also thank my friends and family who have always been an important moral support for me.

Dec. 3rd 2010

Abstract

Numerical Errors and Accuracy-Efficiency Tradeoff in Frequency and Time-Domain Integral Equation Solvers

Guneet Kaur, M.S.E

The University of Texas at Austin, 2010

Supervisor: Ali E. Yilmaz

This thesis presents a detailed study of the numerical errors and the associated accuracy-efficiency tradeoffs encountered in the solution of frequency- and time-domain integral equations. For frequency-domain integral equations, the potential integrals contain singular Green's function kernels and the resulting singular and near-singular integrals must be carefully evaluated, using singularity extraction or cancellation techniques, to ensure the accuracy of the method-of-moments impedance matrix elements. This thesis presents a practical approach based on the progressive Gauss-Patterson quadrature rules for implementing the radial-angular-transform singularity-cancellation method such that all singular and near-singular integrals are evaluated to an

arbitrary pre-specified accuracy. Numerical results for various scattering problems in the high- and low-frequency regimes are presented to quantify the efficiency of the method and contrast it to the singularity extraction method. For time-domain integral equations, the singular Green's function kernels are functions of space and time and sub-domain temporal basis functions rather than entire-domain sinusoidal/Fourier basis functions are used to represent the time variation of currents/fields. This thesis also investigates the accuracy-efficiency tradeoff encountered when choosing sub-domain temporal basis functions by contrasting two prototypical ones: The causal piecewise polynomial interpolatory functions, sometimes called shifted Lagrange interpolants, and the band-limited interpolatory functions based on approximate prolate spheroidal wave functions. It is observed that the former is more efficient for low to moderate accuracy levels and the latter achieves higher, but extrapolation-limited, accuracy levels.

Table of Contents

List of Tables

List of Figures

CHAPTER 1: INTRODUCTION

Integral equation formulations in electromagnetics [1-3] can be solved in frequency or time domain using the method-of-moments (MOM) [4] and marching-on-in-time (MOT) [5] approaches, respectively. There are three major sources of error that affect these solution methods: Modeling, discretization, and numerical errors. Modeling errors are introduced when representing the physical problem by an approximate computational problem, e.g., using a mesh to represent the true geometry. Discretization errors are incurred when expanding unknown currents/fields in terms of a finite number basis functions in space-time. Numerical errors arise when evaluating matrix elements (that typically involve singular and multidimensional integrals) and when solving the resulting matrix equations. Modeling and discretization errors can be controlled by using finer meshes or by using curvilinear elements (and higher order basis functions) to approximate the geometry and currents/fields more accurately [6, 7]. Numerical errors can be controlled by using more advanced quadrature rules for evaluating integrals and novel integral-equation formulations for improving matrix condition numbers [8]. All such error control mechanisms incur additional computational costs. This thesis presents a detailed study of the numerical errors and the associated accuracy-efficiency tradeoffs encountered in the solution of frequency- and time-domain integral equations.

For frequency-domain integral equations, the potential integrals contain singular Green's function kernels. The resulting singular and near-singular integrals must be carefully evaluated to ensure the accuracy of the MOM impedance matrix elements. This can be achieved using two methods: (i) Singularity extraction (SE) method [9-12], where asymptotic forms of Green's functions are subtracted from the integrands before numerical evaluation, analytically integrated, and added back to the numerical integrals.

(ii) Singularity cancellation (SC) method [13-16], where nonsingular integrals are obtained by a change of variables and the resulting integrals are numerically evaluated over transformed domains. For classical MOM solvers that use low-order basis/testing functions and the free-space Green's function, the SE method is simpler, more efficient, and thus more popular; yet, it is impractical when high-order basis functions or more complex Green's functions are used due to a lack of closed form integrals. In contrast, the SC method is straightforward to generalize to these cases but loses efficiency for near-singular integrals, i.e., the integrals corresponding to basis-testing functions that are in close proximity to each other but are non-overlapping. In the SC method, near-singular integrals are computed either by extending the integration domain beyond its original limits and subtracting the contributions from the extended regions [14, 15] or by operating on the original but more complicated domain [16]; the former approach is limited by numerical cancellation errors, the latter by a lack of quadrature rules for arbitrary domains. In both approaches, the quadrature performance depends not only on the original integrand (the basis and Green's functions) but also on the integration domain (the shape and relative locations of the basis/testing functions) and can vary drastically from one integral to the other. Unfortunately, prescriptions for choosing quadrature rules that guarantee a desired accuracy when evaluating the transformed integrals are elusive; this typically leads to unnecessarily high order quadrature rules to be used in the SC method.

This thesis presents a practical numerical integration approach for the radial-angular-transform SC method [15] such that all singular and near-singular MOM integrals are evaluated to an arbitrary pre-specified accuracy. First, general guidelines are presented to determine the distance up to which standard quadrature rules must be replaced by the singularity treatment methods for achieving a pre-specified accuracy.

Second, the transformed versions of the MOM integrals are repeatedly evaluated (using first the least accurate but fastest quadrature rules and then more accurate but slower rules) to obtain error estimates; if the estimated error is below a pre-specified level, the evaluation is terminated.

For time-domain integral equations, the potential integrals are functions of space-time and sub-domain temporal basis functions rather than entire-domain sinusoidal/ Fourier basis functions are used to represent the time variation of currents and fields. The choice of the temporal basis function plays a critical role in the accuracy and efficiency of the MOT solution: It dictates the interpolation, integration, and extrapolation errors and the matrix-fill, memory, and time-marching costs (see Chapter 3 for precise definitions). This thesis investigates the accuracy-efficiency tradeoff encountered when choosing sub-domain temporal basis functions by contrasting two prototypical ones: The causal piecewise polynomial interpolatory functions (CPPIFs) [5, 17-19], sometimes called shifted Lagrange interpolants [18, 19], and the band-limited interpolatory functions (BLIFs) based on approximate prolate spheroidal wave functions [20-22]. The relative merits of CPIFFs and BLIFs are examined by solving various transient scattering problems and measuring the accuracy and efficiency of the MOT solution.

The rest of the thesis is organized as follows. Chapter 2 formulates the two methods for treating the singular potential integrals in the frequency domain, details the problems encountered in the SC method, and the proposed approach for resolving them. It also contrasts the accuracy and computational costs of the proposed SC method to those of a typical SE method. Chapter 3 formulates the MOT solution and analyzes the main sources of errors that directly depend on the temporal basis function. It also presents numerical results and quantifies the accuracy-efficiency tradeoff. Chapter 4 presents the conclusions.

CHAPTER 2: A PRACTICAL IMPLEMENTATION AND COMPARATIVE ASSESSMENT OF THE RADIAL-ANGULAR-TRANSFORM SINGULARITY CANCELLATION METHOD

This chapter first reviews the frequency-domain electric-field integral equation (EFIE) and its MOM solution for a perfect electrically conducting (PEC) surface. It then presents the SE and SC methods in detail and contrasts the accuracy and computational costs of the two methods.

2.1 EFIE

Consider a PEC surface S in free space that is illuminated by a time-harmonic electromagnetic field $\mathbf{E}^{\text{inc}}$. The field $\mathbf{E}^{\text{sca}}$ that is scattered by the surface can be expressed as

$$\mathbf{E}^{\text{sca}}(\mathbf{r}) = -j\omega\mu_0 \iint_S \mathbf{J}(\mathbf{r}')\, g(R)\, dS' + \frac{\nabla}{j\omega\varepsilon_0} \iint_S \nabla' \bullet \mathbf{J}(\mathbf{r}')\, g(R)\, dS' \tag{2.1}$$

Here, ε_0 and μ_0 are the free-space permittivity and permeability, $g(R) = e^{-jk_0 R}/(4\pi R)$ is the free-space Green's function, $k_0 = \omega\sqrt{\mu_0\varepsilon_0}$, $R = |\mathbf{r} - \mathbf{r}'|$, and $\mathbf{J}$ is the surface current density. Let $\hat{n}$ denote the outward directed unit vector normal to S; the EFIE constructed by enforcing the tangential component of the total electric field to vanish on S can be expressed as

$$\hat{n} \times \hat{n} \times \left[\mathbf{E}^{\text{inc}}(\mathbf{r}) + \mathbf{E}^{\text{sca}}(\mathbf{r}) \right] = \mathbf{0} \tag{2.2}$$

In order to find the unknown $\mathbf{J}$, first (2.1) is substituted in (2.2); then, the current is approximated as $\mathbf{J} \cong \sum_{n=1}^{N} I_n \mathbf{S}_n(\mathbf{r})$. Here, $\mathbf{S}_1, ..., \mathbf{S}_N$ are RWG basis functions [23] defined on pairs of triangular patches that discretize S and $I_1, ..., I_N$ are the unknown current coefficients. Next, a linear system of equations is obtained by Galerkin testing and solved; in matrix form, these equations are given as $\mathbf{ZI} = \mathbf{V}$, where the impedance matrix entries are (for $m = 1, ..., N$ and $n = 1, ..., N$)

$$\mathbf{Z}[m,n] = j\omega\mu_0 \iint_S \mathbf{S}_m(\mathbf{r}) \bullet \iint_S \mathbf{S}_n(\mathbf{r}')\, g(R)\, dS' dS + \frac{1}{j\omega\varepsilon_0} \iint_S \nabla \bullet \mathbf{S}_m(\mathbf{r}) \iint_S \nabla' \bullet \mathbf{S}_n(\mathbf{r}') g(R)\, dS' dS \tag{2.3}$$

Because RWG basis functions are used, the inner integrals in (2.3) have the general form $\iint_S g(R)dS'$ and $\iint_S \mathbf{f}(\mathbf{r}')g(R)dS'$, where $\mathbf{f}(\mathbf{p}') = \rho'\hat{}$ is a position vector defined with respect to the free vertex of each patch of an RWG function. Standard Gaussian quadrature rules defined over triangular domains are appropriate for evaluating these integrals when the testing and basis functions are far apart; they are not effective, however, when the functions overlap (integrands are singular) or are close to each other (integrands are near-singular). This is because the standard rules that are designed to integrate polynomials become less accurate (as the integrands cannot be interpolated accurately near a singularity by using polynomials).

2.2 Singular and Near-Singular Integration

The SE and SC methods are detailed next for the singular and near-singular inner integrals in (2.3). The methods are formulated using the vector potential integral for brevity; the corresponding expressions for the scalar potential integral can be obtained by replacing $\mathbf{f}(\mathbf{r}')$ with 1.

2.2.1 Singularity Extraction (SE) Method

In the SE method, analytically integrable asymptotic forms of the Green's functions are subtracted from the integrands; integrated analytically; and added back to the numerical integral:

$$\mathbf{I} = \iint_S \mathbf{f}(\mathbf{r}')g(R)dS' \approx \underbrace{\iint_S \mathbf{f}(\mathbf{r}')\left[g(R) - A(R)\right]dS'}_{\text{Numerical Integration}} + \underbrace{\iint_S \mathbf{f}(\mathbf{r}')A(R)dS'}_{\text{Analytical Integration}} \tag{2.4}$$

Here, $A(R)$ is the asymptotic form; e.g., $A(R) = \sum_{q=-1}^{Q} (-jk_0)^{q+1} R^q \big/ (q+1)!$ for the free-space Green's function. The accuracy of the method depends on the number of terms Q

that are extracted from the Green's function [12]. Unfortunately, the implementation of the SE method is impractical for high-order basis and complex Green's functions for which analytical integrals are generally not available. Note that Gaussian quadrature rules are used for all numerical integrals in the SE method.

2.2.2 Singularity Cancellation (SC) Method

In the SC method, the singular terms in the integrands are canceled out by a variable transformation. The typical steps for the SC method for planar source patches are as follows (for extensions to curvilinear patches, see [33]): First, the testing point $\mathbf{r}$ is projected onto the plane of the source patch with vertices $(\mathbf{r}_1', \mathbf{r}_2', \mathbf{r}_3')$ and the projection distance is denoted as d; then, the source patch is divided into sub-triangles about the projected point $\mathbf{r}_p$ (the integration domain is extended beyond the source patch when $\mathbf{r}_p$ is outside of it [Fig. 2.1(a)]). Second, to evaluate the integral over each of these sub-triangles, a local Cartesian coordinate system $(\tilde{x}, \tilde{y}, \tilde{z})$ [13, 14] or polar coordinate system $(\tilde{\rho}, \tilde{\phi}, \tilde{z})$ [15] with origin at $\mathbf{r}_p$ is introduced. The axes of the local coordinate system is defined according to some rule with respect to the source patch; e.g., a local coordinate system for one of the sub-triangles of Fig. 2.1(a) is shown in Fig. 2.1(b), where the $\tilde{z}$ is defined as the direction normal to the plane of the source patch and $\tilde{x}$ is defined in the direction parallel to the sub-triangle's edge that is opposite to $\mathbf{r}_p$. The integrals over each of the three sub-triangles can be expressed as (for $i = 1,2,3$)

$$\mathbf{I}^i = \begin{cases} \displaystyle\int_{\tilde{y}_{\mathrm{L}}^i}^{\tilde{y}_{\mathrm{U}}^i} \int_{\tilde{x}_{\mathrm{L}}^i}^{\tilde{x}_{\mathrm{U}}^i} \mathbf{f}(\tilde{\mathbf{r}}') g(R) d\tilde{x} d\tilde{y}; & \text{Cartesian coordinates} \\ \displaystyle\int_{\tilde{\phi}_{\mathrm{L}}^i}^{\tilde{\phi}_{\mathrm{U}}^i} \int_{\tilde{\rho}_{\mathrm{L}}^i}^{\tilde{\rho}_{\mathrm{U}}^i} \mathbf{f}(\tilde{\mathbf{r}}') g(R) \tilde{\rho} d\tilde{\rho} d\tilde{\phi}; & \text{Polar coordinates} \end{cases} \tag{2.5}$$

Third, the integration variables are transformed as $(\tilde{x}, \tilde{y}) \to (v_1, v_2)$ or $(\tilde{\rho}, \tilde{\phi}) \to (v_1, v_2)$

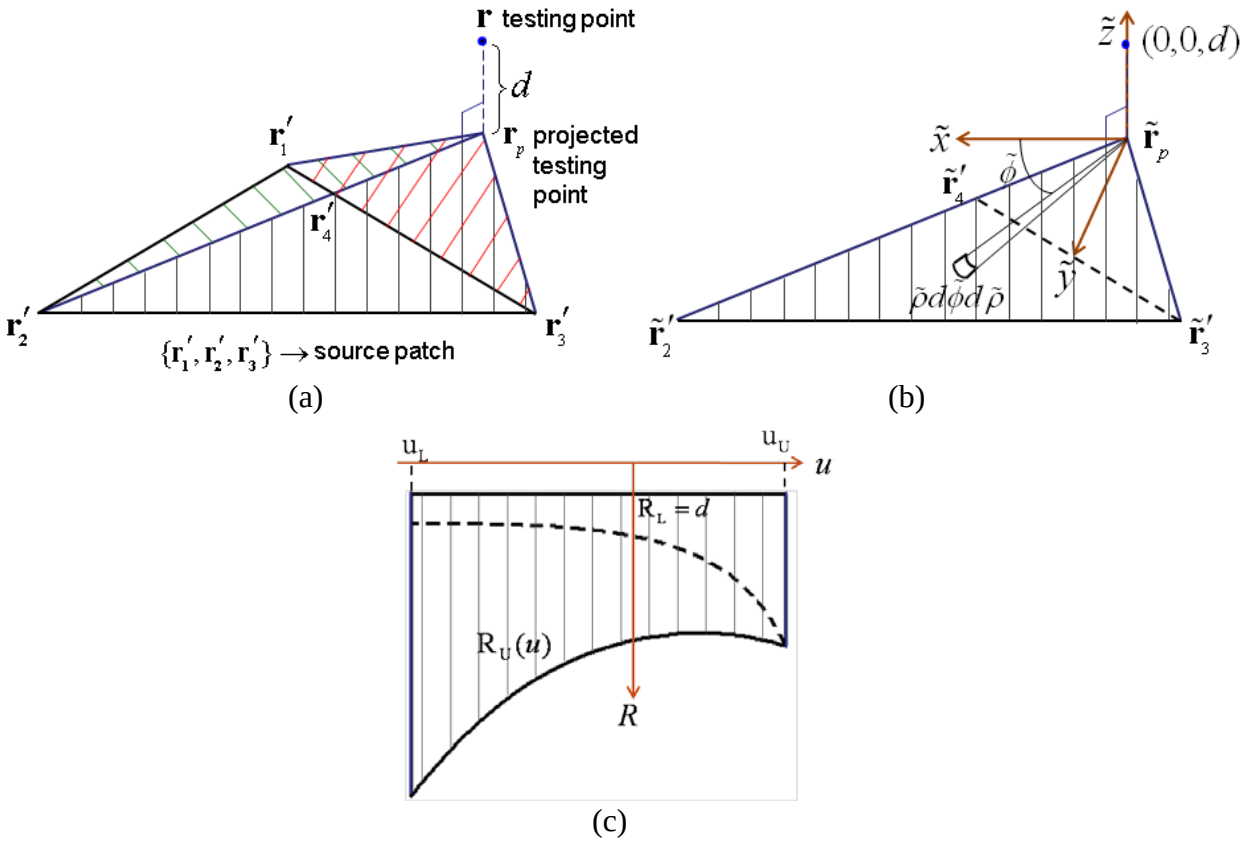

Figure 2.1: SC method for a triangular source patch. (a) Projected testing point and the three sub-triangles. When $\mathbf{r}_p$ lies outside the source patch, the integration domain is extended outside the source patch. (b) A local Cartesian and polar coordinate system for the subtriangle with vertices $(\tilde{\mathbf{r}}_p, \tilde{\mathbf{r}}'_2, \tilde{\mathbf{r}}'_3)$. The dashed line shows the boundary of the source patch. (c) Transformed coordinate system and integration domain for the radial-angular transform SC method corresponding to the sub-triangle in (b).

such that the Jacobian $J(v_1, v_2)$ of the transformation cancels the singularity in the integrand:

$$\mathbf{I}^i = \int_{v_{1\mathrm{L}}^i}^{v_{1\mathrm{U}}^i} \int_{v_{2\mathrm{L}}^i}^{v_{2\mathrm{U}}^i} \mathbf{f}(\tilde{\mathbf{r}}') g(R) J(v_1, v_2) dv_1 dv_2 \tag{2.6}$$

Fourth and last, the integrals are evaluated numerically over the transformed domain. Here, the subscript L (U) indicates the lower (upper) integration limit for the corresponding coordinate variable.

Various variable transforms are used for the SC method. One of the most common is the Duffy transform [13, 24], which is effective for singular integrals but not for near-singular integrals because the derivatives of the transformed integrand are singular when $d \neq 0$. Two other transforms have been proposed recently [14, 15]: The *arcsinh* transform [14] overcomes the limitation of the Duffy transform for near-singular integrals; however, the transformed domain is very sensitive to d when it is small. In comparison, the radial-angular transform [15] not only yields a smooth transformed integrand but also a transformed domain that is insensitive to d. Henceforth, the radial-angular transform is used in this thesis; specifically, a polar coordinate system is used for the local coordinates and the variables are transformed as $(\tilde{\rho},\tilde{\phi}) \to (R,u)$ [Fig. 2.1(c)]:

$$\begin{gathered} R = \sqrt{\tilde{\rho}^2 + \tilde{z}^2} \qquad u = \ln\tan\left(\frac{\tilde{\phi}}{2}\right) \qquad J(R,u) = \frac{R}{\cosh u} \\ R_{\mathrm{L}}^i = 0 \qquad u_{\mathrm{L}}^i = \ln\tan\left(\frac{\tilde{\phi}_{\mathrm{L}}^i}{2}\right) \quad R_{\mathrm{U}}^i(u) = \sqrt{(\tilde{\rho}_{\mathrm{U}}^i)^2 + \tilde{z}^2} \quad u_{\mathrm{U}}^i = \ln\tan\left(\frac{\tilde{\phi}_{\mathrm{U}}^i}{2}\right) \end{gathered} \tag{2.7}$$

Here, the radial transform removes the singularity and the angular transform makes the integrand smoother with angular variations. As mentioned in Chapter 1, the above SC method is inefficient for near-singular integrals since it relies on the cancellation of the contributions from the extended region of integration that lies outside the source patch. It is natural to address this issue by integrating only over the source domain [16]; that is by expressing the lower limit of the radial integration in (2.7) as $R_{\mathrm{L}}^i(u) = \sqrt{(\tilde{\rho}_{\mathrm{L}}^i)^2 + \tilde{z}^2}$ [Fig. 2(a)]. While this "adaptive radial-angular-transform" [16] avoids the cancellation errors and unnecessary computations outside the source domain, it makes the transformed integration domain more irregular [Fig. 2(b)] and a more complex function of the relative orientation of the testing point with respect to the source patch. As a result, simple

rules/tables that determine the optimum quadrature rules (with minimum number of points) for a pre-specified level of accuracy cannot be defined as in [15].

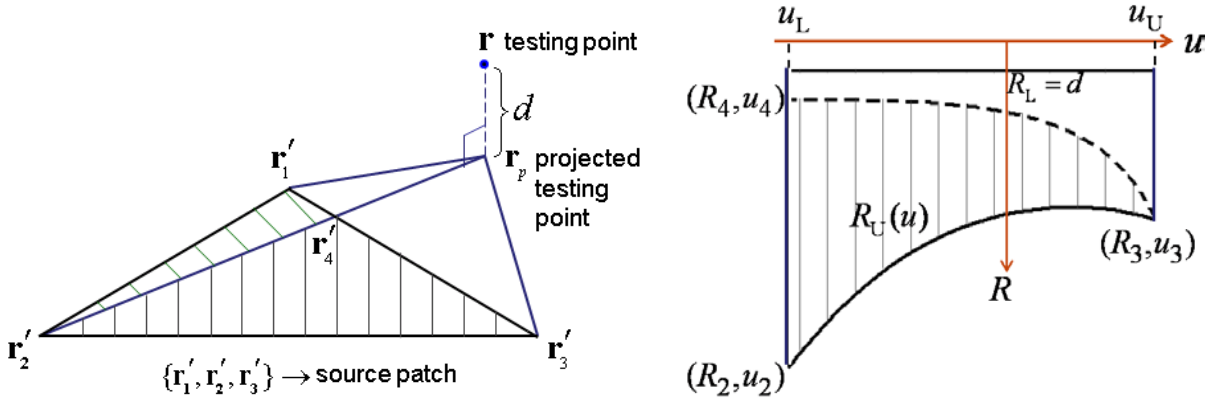

(a) (b)

Figure 2.2: Adaptive integration for the SC method. (a) Projected testing point and the two sub-triangles. The integration domain is not extended outside the source patch. (b) Transformed coordinate system and integration domain for the sub-triangle with vertices $(\mathbf{r}_p, \mathbf{r}_2', \mathbf{r}_3')$

2.3 Practical Issues

In theory, the SC method can be used to compute all impedance matrix entries to arbitrary accuracy (assuming infinite precision arithmetic is available). In practice, however, it is desirable to achieve a pre-specified but variable/controllable level of integration error. This "target error level" is determined by finite computational resources (efficiency constraints) and by other sources of computation and data errors; thus, it is generally problem specific. Two questions must be answered when computing the impedance matrix entries to pre-specified error levels: (i) Which matrix entries should be considered near singular and which ones should be computed using standard quadrature rules? (ii) Which quadrature rules should be used for computing the transformed integral in (2.6)? This section presents a detailed discussion of these issues.

2.3.1 Singularity Cancellation Distance

To determine which impedance matrix entries should be evaluated using standard Gaussian quadrature rules and which ones should be evaluated using the SC method, a distance criterion is used. Let R_{mn} denote the minimum distance between the functions $\mathbf{S}_m$ and $\mathbf{S}_n$ (practically, R_{mn} is found approximately by computing the distances from quadrature points on each testing patch to the vertices of each source patch and finding the minimum). If R_{mn} is less than the "SC distance" R_n^{SC}, then $\mathbf{Z}[m,n]$ is evaluated using the SC method. The SC distance is a function of the desired accuracy level and the source-patch geometry (e.g., shape and relative size compared to the wavelength of interest). In the following, the accuracies of standard quadrature rules are quantified for the integral $\mathbf{I} = I_x\hat{x} + I_y\hat{y}$ given in (2.4) when the source patch is $\mathbf{r}_1' = (0,0,0), \mathbf{r}_2' = (1,0,0), \mathbf{r}_3' = (0,1,0)$ and the observer point is $\mathbf{r} = (0, y, 0)$. The relative error in each component is defined as

$$\mathrm{err}_{\{x,y\}} = \frac{\left| I_{\{x,y\}} - I_{\{x,y\}}^{\mathrm{ref}} \right|}{\left| I_{\{x,y\}}^{\mathrm{ref}} \right|} \tag{2.8}$$

where the reference integral $\mathbf{I}^{\mathrm{ref}}$ is computed with the SC method using a nested one-dimensional Gaussian quadrature rule to evaluate the transformed integral: The 200-point rule is used to evaluate the outer angular integral and for each of the 200 angles, the 200-point rule is used to evaluate the inner radial integral (Section 2.3.2). To demonstrate the properties of the SC distance, the maximum error in the components of $\mathbf{I}$ is plotted in Fig. 2.3 versus the normalized distance $|\mathbf{r} - \mathbf{r}_3'| / l^{\max}$ at several frequencies, where $l^{\max}$ is the maximum edge length of the source patch. Fig. 2.3 shows that, as expected, standard quadrature rules are inaccurate for small distances and accurate for large distances. (Notice that the error begins to grow for higher order rules at larger distances; this is because the reference SC method loses accuracy due to numerical errors in

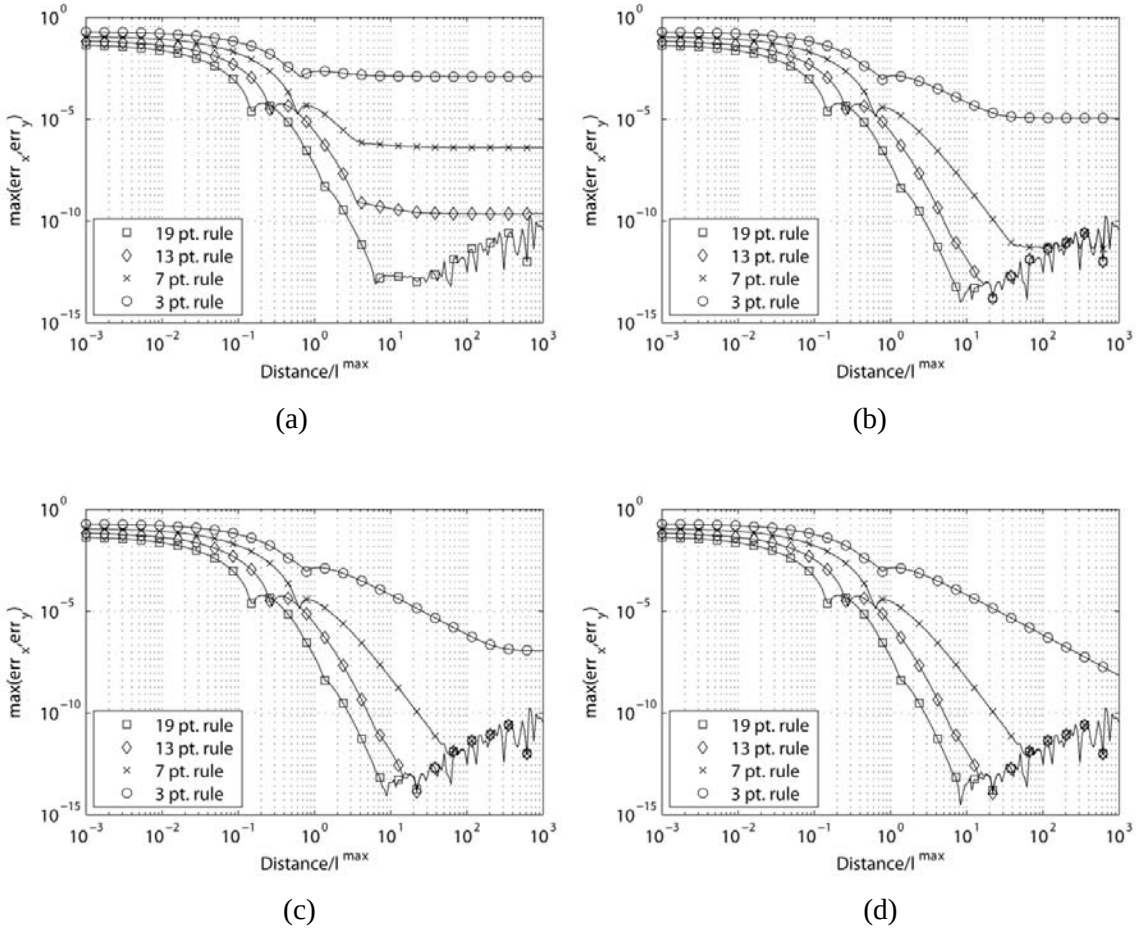

Figure 2.3: The relative error using standard quadrature rules versus the testing-point distance for the source patch in Fig. 4 at (a) 30 MHz (b) 3 MHz (c) 300 kHz (d) 3 kHz.

evaluating small angles. Indeed, the SC method is not only costlier but also less accurate than standard quadrature rules at large distances.) In all cases, the quadrature rule accuracy improves as the order of the rule is increased or the frequency is decreased; at smaller distances, however, the improvement is negligible and the error is insensitive to both the order and the frequency. As expected standard quadrature rules are ineffective at smaller distances. Importantly, Fig. 2.3 also shows that, the SC distance is insensitive to frequency of interest; e.g., for 10^{-6} error level, the SC distance is always about $3.5\,l^{\max}$.

This implies that the smaller the source patch, the smaller is the corresponding SC distance for a fixed frequency. Although only one sample case is shown here, extensive tests were conducted and also showed that the above observations hold for different source patch shapes and relative orientations of the observer point; indeed, the SC distance is found to be primarily a function of the maximum edge length of the source patch, i.e., $R_n^{\mathrm{SC}} = \alpha l_n^{\max}$.

2.3.2 Numerical Integration

As argued in Section 2.2, quadrature rules for evaluating the transformed integrals in the SC transform cannot be determined using simple rules/tables; thus, numerical integration schemes that provide on-the-fly error estimates must be used for selecting the quadrature rules. One alternative is to use adaptive integration [25]: Recursively subdivide the domain until the integration error converges to a pre-specified tolerance level in each of the subintervals. Although these rules can integrate non-smooth integrands and allow the use of high order quadrature rules, they are costly, especially for smooth integrands, as the evaluation points for the previous and new subintervals do not coincide. Another alternative is to use progressive quadrature rules that do not subdivide the domain but instead progressively increase the quadrature order. The high order rules re-use the function values for the low order estimates by adding new quadrature points to the previous ones. The Gauss-Patterson rules (unlike the Gauss-Kronrod rules that are in pairs) consist of a set of nested rules that use $(1,3,7,15,31,63,127,255)$ points; the new points are successively added to the previous ones and thus provide lower errors without subdividing the interval. Naturally, these rules are not as accurate as the corresponding non-progressive rules, e.g., the $4n+3$ point Gauss-Patterson rule provides exact integration for up to $6n+4$ degree polynomials, in contrast to the $8n+5$ degree obtained

from the corresponding Gaussian rule. Hence, there is a tradeoff between the progressive property and the order of integration. Because the transformed integrand in the SC method is smooth, it is expected (and confirmed through numerical experiments not shown here) that the Gauss-Patterson rules are more efficient than adaptive quadrature rules for evaluating the impedance matrix entries.

2.4 Numerical Results

This section presents numerical results that compare the accuracy and efficiency of the two methods for computing the singular and near-singular integrals. First, the SE and SC methods are contrasted for a specific source patch and several testing points. Then, both methods are implemented in a MOM solver and are compared when the solver is applied to different scattering problems. In the latter comparison, the performance of progressive Gauss-Patterson and (static) Gaussian quadrature rules are also contrasted for the SC method. In all scattering problems, the MOM equations are diagonally preconditioned and solved using a transpose-free quasiminimal residual (TFQMR) iterative solver [34] that is terminated when the relative residual error is lower than 10^{-6}.

2.4.1 Sample Integral

To compare the accuracy of the SE and SC methods, the integral in (2.4) is evaluated for the source patch described in Section 2.3.1 and three testing points; the testing points coincide with one of the quadrature points of a 19-point Gaussian rule on the same patch and two near patches (Fig. 2.4). Integrals for all three cases are evaluated using both the adaptive radial-angular-transform SC method and SE method (the $q = -1,1,3$ terms in the Taylor expansion after (2.4) are extracted and the analytical

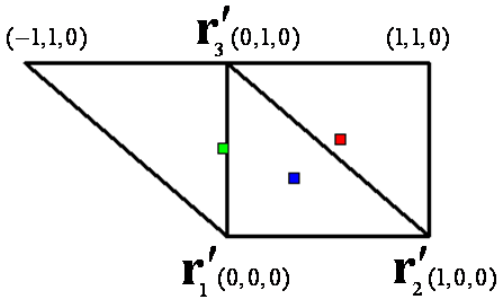

Figure 2.4: A source patch that is an isosceles unit triangle and three testing points marked in blue, red, and green.

expressions in [12] are used). The result from the radial-angular-transform SC method that uses 200-point Gaussian rules in both radial and angular directions is used as a reference. The error as defined in (2.8) is shown versus the number of quadrature points in Fig. 2.5. The figure shows that the SE method is limited in accuracy when only the $q=-1$ term is extracted; yet, it can achieve arbitrary accuracy when additional terms are extracted. For singular integrals, the two methods are comparable; for near singular integrals, the SC method requires many more quadrature points. For example, in Fig. 2.5(c), the SC method requires about 10 times the number of quadrature points to achieve 10^{-6} error; in this case, both the lower radial limit and the RWG position vector along the lower radial limit vary sharply with respect to the transverse variable, and thus a higher number of quadrature points is required to resolve this variation. It is clear from Fig. 2.5 that the SC method generally requires more quadrature points than the SE method to achieve the same accuracy and is thus less efficient. Next, the performance of the SE and SC method are investigated when solving various scattering problems.

2.4.2 Sphere

First, the methods are validated by analyzing scattering from a sphere and comparing results to the ones from the Mie series solution. The sphere has a radius of $1\,\mathrm{m}$ and the

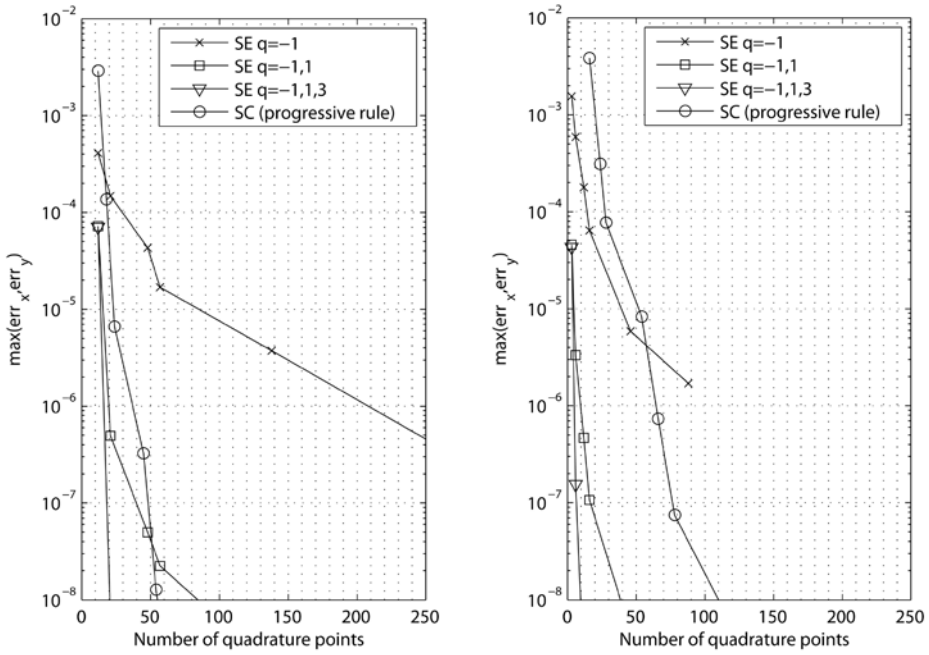

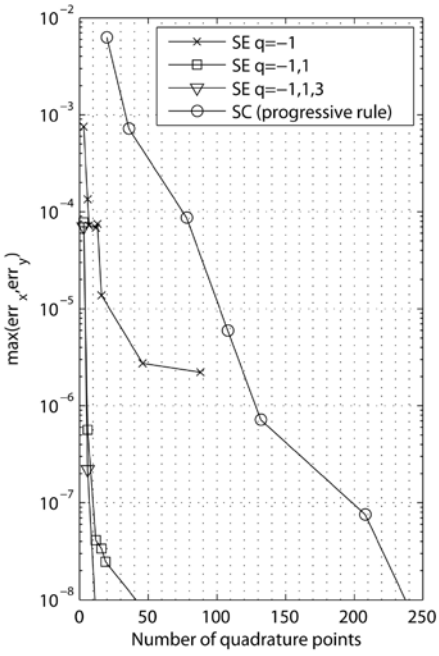

Figure 2.5: The relative error using the SC and SE methods for the patch in Fig. 2.4 and the testing point marked in (a) blue, (b) red, and (c) green.

surface current density is discretized using $N = 3384$ RWG basis functions with an average edge length of ~0.11 m. The sphere is excited by an $\hat{x}$–polarized plane wave propagating in $-\hat{z}$ direction and the HH-polarized bistatic radar cross section (RCS) $\sigma_{\theta\theta}$ is calculated along the $\phi = 0$ cut (the *x*-*z* plane) at 300 MHz and 150 kHz (Fig. 2.6) (the sphere radius is ~ 1 and $\sim 5 \times 10^{-4}$ wavelengths at these frequencies). Fig. 2.6 shows that the results from all methods are accurate in the high-frequency regime but the SE method with one term extraction is not accurate enough in the low-frequency regime. In these simulations, the 19-point Gaussian quadrature rule was used for the testing (outer) integrals and the SC/SE quadrature rules (and the SC distance) were chosen to yield 5 or more correct digits for all impedance matrix entries, i.e., the maximum relative error in inner integrals in (2.3) as defined in (2.8) is 10^{-5}. It was observed that in the 300 MHz simulation (and in the high-frequency regime in general) reducing the integration error to lower than 10^{-5} does not reduce the error in the RCS further. This is because the total solution error is dominated by other error sources, e.g., the (surface) modeling and (current) discretization errors, once the integration error falls below this level. In contrast, at lower frequencies, the integration errors are more dominant (due to the EFIE low-frequency breakdown [35] and the reduced discretization error) and reducing the integration errors can reduce the total error significantly.

To further study the effects of integration errors, scattering from the same sphere is analyzed by using a finer mesh and by varying the frequency of interest. The surface current density is discretized using $N = 7431$ RWG basis functions with an average edge length of $l_{\text{avg}} \sim 2.7$ mm. The relative error in RCS is quantified as:

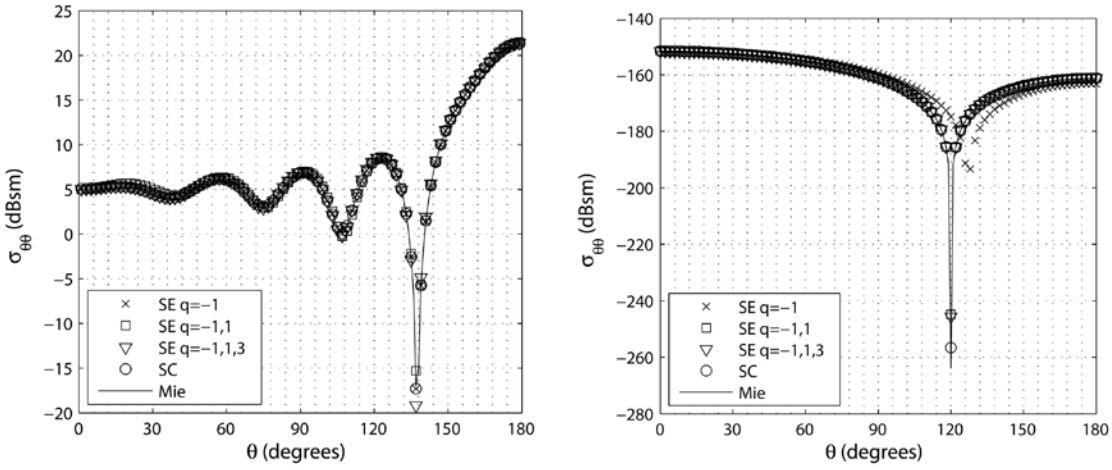

Figure 2.6: Bistatic RCS for the $1\,\mathrm{m}$ sphere at frequencies (a) $300\ \mathrm{MHz}$ and (b) $150\ \mathrm{kHz}$.

$$\mathrm{err}_{\mathrm{RCS}} = \sqrt{\frac{\int_0^{\pi}\left(\sigma_{\theta\theta}(\theta,\phi=0)-\sigma_{\theta\theta}^{\mathrm{Mie}}(\theta,\phi=0)\right)^2 d\theta}{\int_0^{\pi}\left(\sigma_{\theta\theta}^{\mathrm{Mie}}(\theta,\phi=0)\right)^2 d\theta}} \tag{2.9}$$

where $\sigma_{\theta\theta}^{\mathrm{Mie}}$ is the Mie series reference. The error, the number of iterations needed for convergence, and the time needed to fill the singular and near-singular impedance matrix entries are plotted for the SE and SC methods in Fig. 2.7. Two sets of data are obtained for the SC method: One using the proposed adaptive Gauss-Patterson rules with a pre-specified tolerance and the other using a fixed/static Gaussian rule found by trial and error. Fig. 2.7 shows that the accuracy of the SE and SC methods are similar in the high-frequency regime. It is observed that the SC method using progressive quadrature and the higher order SE method have comparable results and delay the low-frequency breakdown frequency about two orders of magnitude as compared to the lowest order SE method. There is premature convergence of the iterative solver at lower frequencies as confirmed by the increase in the RCS error. Fig. 2.7(c) shows that the fill time increases as the frequency is lowered, as should be expected. Moreover, the proposed SC method with progressive quadrature is about 10^2 more costly than the SE method.

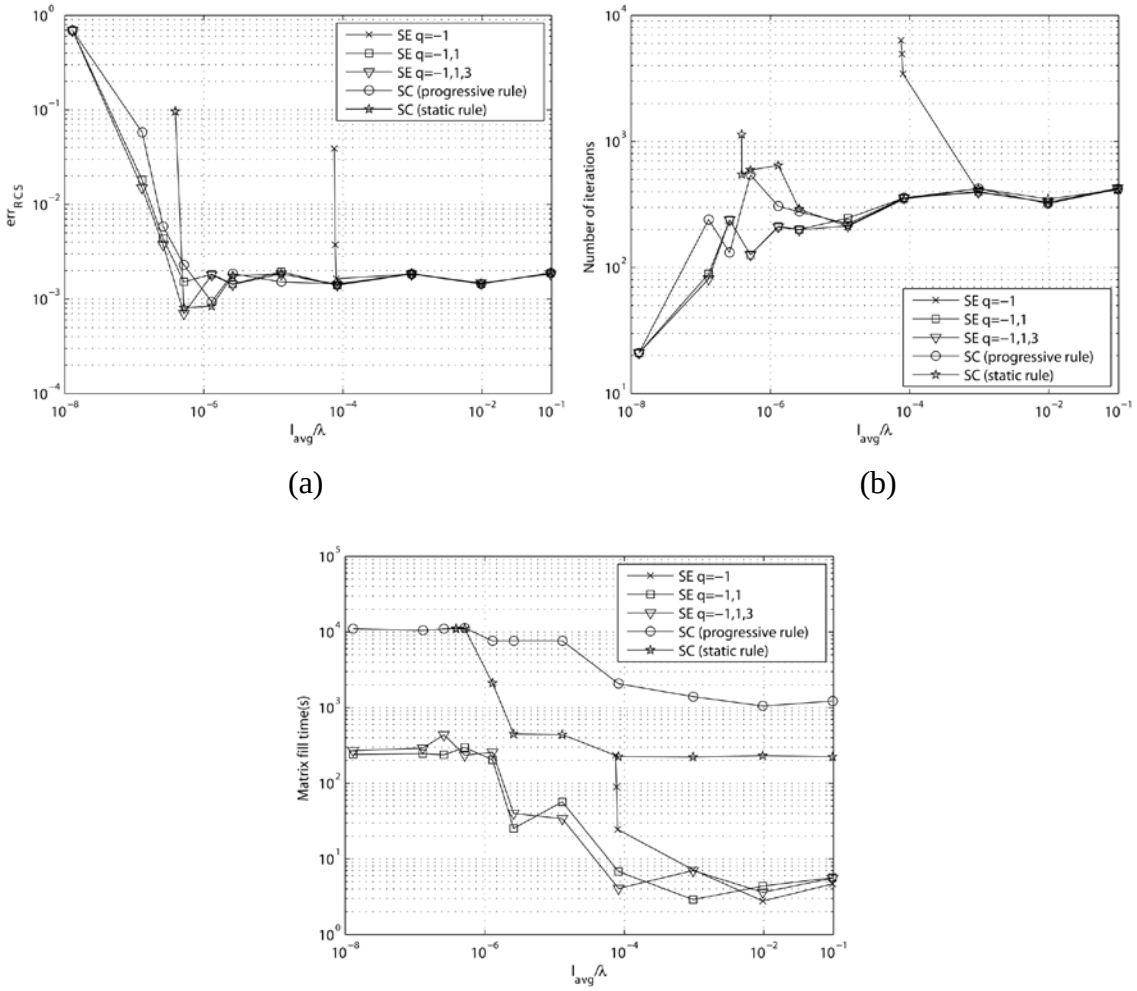

Figure 2.7: Results for the MOM solution of scattering from sphere discretized with $N = 7431$ over a frequency range: (a) $\mathrm{err}_{\mathrm{RCS}}$, (b) number of iterations, and (c) matrix fill time for all singular and near-singular matrix entries.

The number of quadrature points used for the evaluation of all integrals in SE simulations and non-singular integrals in SC simulations is listed in Table 2.1 for different frequency ranges. This table also lists the pre-specified accuracy in terms of the number of accurate digits, based on which the SC distance is determined for all simulations and the stopping criterion is determined for the singular and near-singular integrals for SC simulations using progressive rules. For the SC simulations using a static rule, the same fixed

Gaussian rule is used for all the singular and near-singular integrals in a particular simulation, starting with (3,6) and increased up to (15,30) point rule for the (radial, angular) integral at different frequencies (Table 2.2).

Method	Frequency range	Pre-specified accuracy (number of digits)	Number of quadrature points	
			Source (inner)	Testing (outer)
SE $q=-1$	$l_{\text{avg}}/\lambda > 10^{-4}$	5	7	7
	$8.25\times10^{-5} < l_{\text{avg}}/\lambda < 10^{-4}$	7	13	13
	$7.75\times10^{-5} < l_{\text{avg}}/\lambda < 8.25\times10^{-5}$	9	19	19
	$l_{\text{avg}}/\lambda < 7.75\times10^{-5}$	9	46	19
SE $q=-1,1$ and $q=-1,1,3$	$l_{\text{avg}}/\lambda > 8.25\times10^{-5}$	5	7	7
	$2\times10^{-6} < l_{\text{avg}}/\lambda < 8.25\times10^{-5}$	7	13	13
	$5.0\times10^{-7} < l_{\text{avg}}/\lambda < 2.0\times10^{-6}$	9	19	19
	$l_{\text{avg}}/\lambda < 5.0\times10^{-7}$	9	46	19
SC (progressive rule)	$l_{\text{avg}}/\lambda > 8.25\times10^{-5}$	5	7	7
	$10^{-6} < l_{\text{avg}}/\lambda < 8.25\times10^{-5}$	7	13	13
	$l_{\text{avg}}/\lambda < 10^{-6}$	9	19	19

Table 2.1: Quadrature rules used for sphere results in Fig. 2.7.

Method	Frequency range	Number of quadrature points	
		Source Total (Radial,Angular)	Testing (outer)
SC (static rule)	$l_{\text{avg}}/\lambda > 8.25\times10^{-5}$	18 (3,6)	7
	$10^{-6} < l_{\text{avg}}/\lambda < 8.25\times10^{-5}$	18 (3,6)	13
	$3.0\times10^{-7} < l_{\text{avg}}/\lambda < 10^{-6}$	105 (7,15)	13
	$l_{\text{avg}}/\lambda < 3.0\times10^{-7}$	450 (15,30)	19

Table 2.2: Quadrature rules used for sphere results in Fig. 2.7.

2.4.3 Almond

To demonstrate the generality of these observations, a NASA almond [26] is simulated using $N = 19467$ RWG basis functions. The parameters that govern accuracy were set in a similar way as the previous example. Tables 2.3 and 2.4 list the number of quadrature point rules used by the different methods at various frequencies. Figs. 2.8(a)-(b) plot the number of iterations taken by the iterative solver for convergence and the time taken to fill the singular and near-singular matrix entries over a range of frequencies. Here again, the convergence of all methods is similar in the high frequency range and the lowest order SE method breaks down at relatively higher frequencies. Fig. 2.8(b) shows that the matrix fill time needed for the static SC method overshoots the time for the SC method with progressive quadrature at a relatively high frequency compared to the previous example and illustrates the advantages of the progressive quadrature rule for a general scatterer.

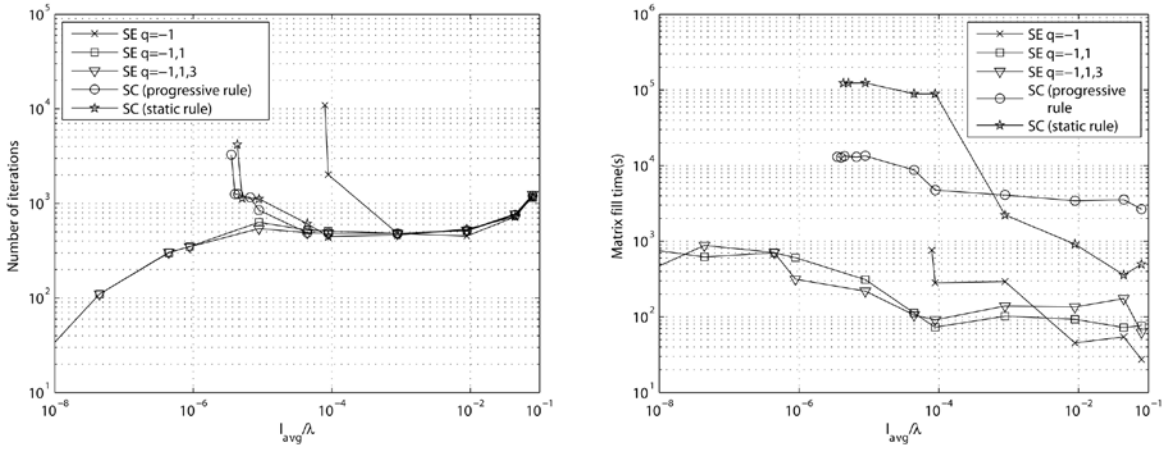

(a) (b)

Figure 2.8: Results for the MOM solution of scattering from NASA almond discretized with $N = 19467$ over a frequency range: (a) number of iterations and (b) matrix fill time for the singular and near-singular elements.

Method	Frequency range	Pre-specified Accuracy (number of digits)	Number of quadrature points	
			Source (inner)	Testing (outer)
SE $q=-1$	$l_{\text{avg}}/\lambda > 10^{-3}$	5	7	7
	$10^{-3} < l_{\text{avg}}/\lambda < 10^{-4}$	7	13	13
	$8.0\times10^{-5} < l_{\text{avg}}/\lambda < 10^{-4}$	9	19	19
	$l_{\text{avg}}/\lambda < 8.0\times10^{-5}$	9	46	19
SE $q=-1,1$ and $q=-1,1,3$	$l_{\text{avg}}/\lambda > 8.0\times10^{-5}$	5	7	7
	$10^{-6} < l_{\text{avg}}/\lambda < 8.0\times10^{-5}$	7	13	13
	$5.0\times10^{-7} < l_{\text{avg}}/\lambda < 10^{-6}$	9	19	19
	$l_{\text{avg}}/\lambda < 5.0\times10^{-7}$	9	46	19
SC (progressive rule)	$l_{\text{avg}}/\lambda > 8.0\times10^{-5}$	5	7	7
	$10^{-6} < l_{\text{avg}}/\lambda < 8.0\times10^{-5}$	7	13	13
	$l_{\text{avg}}/\lambda < 10^{-6}$	9	19	19

Table 2.3: Quadrature rules used for almond results in Fig. 2.8.

Method	Frequency range	Number of quadrature points	
		Source Total (Radial,Angular)	Testing (outer)
SC (static)	$l_{\text{avg}}/\lambda > 10^{-3}$	18 (3,6)	7
	$10^{-4} < l_{\text{avg}}/\lambda < 10^{-3}$	105 (7,15)	13
	$10^{-6} < l_{\text{avg}}/\lambda < 10^{-4}$	1800 (30,60)	19
	$l_{\text{avg}}/\lambda < 10^{-6}$	2450 (35,70)	19

Table 2.4: Quadrature rules used for almond results in Fig. 2.8.

2.5 Summary

This chapter discussed and addressed the practical issues encountered in the implementation of the SC method in a MOM solver. It also compared SC method with the classic SE method by evaluating their performance in an EFIE formulation based MOM solver. It is observed that accuracy achievable through SE is limited by the number

of terms extracted and evaluated analytically. The SE method is more efficient and thus a preferable choice over the SC method for cases when either the integration error levels up to $\sim 10^{-5}$ are accurate enough, for example, for scattering problems in the high frequency regime solved using lower order spatial basis functions, or when high accuracies are desired and achievable through analytical evaluation of higher extracted terms. Singularity Cancellation on the other hand, being a general method, will be a preferable choice for problems involving complex Green's functions and higher order basis functions, where higher order SE might not be available.

CHAPTER 3: ACCURACY-EFFICIENCY TRADEOFF OF TEMPORAL BASIS FUNCTIONS FOR MARCHING ON IN TIME SOLVERS

This chapter first reviews the formulation of the CFIE, its MOT solution, and the two classes of temporal basis functions. Then it presents a detailed analysis of the relevant errors.

3.1 CFIE

Consider a perfect electrically conducting surface S residing in free space and illuminated by an incident transient electromagnetic field $\{\mathbf{E}^{\text{inc}}, \mathbf{H}^{\text{inc}}\}$ that is essentially band-limited to frequencies $f \le f_{\max}$ and vanishes on S for $t \le 0$. The CFIE is constructed by enforcing the time derivatives of the tangential boundary conditions on S and then linearly combining the resulting equations [18, 27]:

$$\begin{aligned}(1-\alpha)\hat{n}\times\frac{\partial}{\partial t}\mathbf{H}^{\text{inc}}(\mathbf{r},t)-\frac{\alpha}{\eta_0}\hat{n}\times\hat{n}\times\frac{\partial}{\partial t}\mathbf{E}^{\text{inc}}(\mathbf{r},t) = (1-\alpha)\frac{\partial}{\partial t}\left[\mathbf{J}(\mathbf{r},t)-\frac{1}{\mu_0}\hat{n}\times\nabla\times\mathbf{A}(\mathbf{r},t)\right] \\ -\frac{\alpha}{\eta_0}\hat{n}\times\hat{n}\times\frac{\partial}{\partial t}\left[\frac{\partial}{\partial t}\mathbf{A}(\mathbf{r},t)+\nabla\phi(\mathbf{r},t)\right]\end{aligned} \tag{3.1}$$

Here, $\hat{n}$ is the outward directed unit vector normal to S, α is a real constant between zero and one, and μ_0, ε_0, and $\eta_0 = (\mu_0/\varepsilon_0)^{1/2}$ are the free-space permeability, permittivity, and intrinsic impedance, respectively. To solve the CFIE, first the vector potential $\mathbf{A}$ and scalar potential ϕ are expressed in terms of the unknown surface current density $\mathbf{J}$. Then, $\mathbf{J}$ is discretized using N_s spatial basis functions $\mathbf{S}_1,\ldots,\mathbf{S}_{N_s}$ and N_t temporal basis functions $T_1,\ldots,T_{N_t}$:

$$\mathbf{J}(\mathbf{r},t) \cong \sum_{k'=1}^{N_S}\mathbf{S}_{k'}(\mathbf{r})J_{k'}(t) \cong \sum_{k'=1}^{N_S}\mathbf{S}_{k'}(\mathbf{r})\sum_{l'=1}^{N_t}I_{k',l'}T_{l'}(t) \tag{3.2}$$

Here, $J_{k'}$ denotes the time variation of $\mathbf{S}_{k'}$ and $I_{k',l'}$ denotes the unknown current coefficient associated with the space-time basis function $\mathbf{S}_{k'}T_{l'}$. Typically,

$T_{l'} = T(t - l'\Delta t)$, where Δt is the time step size, T is an interpolatory basis function that is zero outside the sub-domain $t_s \Delta t < t < t_e \Delta t$. The time step size is constrained by $f_{\max}$, the maximum frequency of interest according to the sampling theorem; i.e., Δt must be chosen such that $\beta = f_{\max} \Delta t < 0.5$. Substituting (2.2) in (2.1) and applying Galerkin testing in space at times $t = \Delta t, ..., N_t \Delta t$ yields the system of equations

$$\sum_{l'=1}^{N_t} \mathbf{Z}_{l-l'} \mathbf{I}_{l'} = \mathbf{V}_l^{\text{inc}} \quad \text{for } l = 1, ..., N_t \tag{3.3}$$

The entries of the vectors $\mathbf{I}_{l'}$, $\mathbf{V}_l^{\text{inc}}$, and the matrix $\mathbf{Z}_{l-l'}$ are

$$\begin{aligned} Z_{l-l'}[k,k'] = (1-\alpha) & \left(\begin{array}{l} \iint_{S_k} \mathbf{S}_k(\mathbf{r}) \cdot \mathbf{S}_{k'}(\mathbf{r}') \frac{\partial}{\partial t} T\left(t - R/c_0\right) dS \\ + \iint_{S_k} \left(\hat{n} \times \mathbf{S}_k(\mathbf{r})\right) \cdot \nabla \times \iint_{S_{k'}} \mathbf{S}_{k'}(\mathbf{r}') \frac{\partial}{\partial t} \frac{T\left(t - R/c_0\right)}{4\pi R} dS' dS \end{array} \right)_{t=(l-l')\Delta t} \\ + \frac{\alpha}{\eta_0} & \left(\begin{array}{l} \mu_0 \iint_{S_k} \mathbf{S}_k(\mathbf{r}) \cdot \iint_{S_{k'}} \frac{\partial^2}{\partial t^2} \frac{T\left(t - R/c_0\right)}{4\pi R} \mathbf{S}_{k'}(\mathbf{r}') dS' dS \\ + \frac{1}{\varepsilon_0} \iint_{S_k} \nabla \cdot \mathbf{S}_k(\mathbf{r}) \iint_{S_{k'}} \frac{T\left(t - R/c_0\right) \nabla' \cdot \mathbf{S}_{k'}(\mathbf{r}')}{4\pi R} dS' dS \end{array} \right)_{t=(l-l')\Delta t} \end{aligned} \tag{3.4}$$

$$\mathbf{I}_{l'}[k'] = I_{k',l'}; \quad \mathbf{V}_l^{\text{inc}}[k] = \iint_{S_k} \mathbf{S}_k(\mathbf{r}) \cdot \left((1-\alpha) \hat{n} \times \frac{\partial}{\partial t} \mathbf{H}^{\text{inc}}(\mathbf{r}, t) + \frac{\alpha}{\eta_0} \frac{\partial}{\partial t} \mathbf{E}^{\text{inc}}(\mathbf{r}, t) \right) dS \Bigg|_{t=l\Delta t} \tag{3.5}$$

for $1 \le k, k' \le N_s$. Here, $c_0 = (\varepsilon_0 \mu_0)^{-1/2}$ is the speed of light, $R = |\mathbf{r} - \mathbf{r}'|$ is the distance between the source point $\mathbf{r}'$ and the observation point $\mathbf{r}$, and S_k denotes the support/domain of the function $\mathbf{S}_k$.

The system of equations in (3.3) can be solved efficiently if $\mathbf{Z}_{1-N_t}, ..., \mathbf{Z}_{-1} = 0$; this is sometimes called the "march criterion" [20]. When the march criterion is met, the unknown coefficients $\mathbf{I}_l$ can be found by solving an equation of the form $\mathbf{Z}_0 \mathbf{I}_l = \mathbf{V}_l^{\text{inc}} - \sum_{l'=1}^{l-1} \mathbf{Z}_{l-l'} \mathbf{I}_{l'}$ at each time step $l = 1, ..., N_t$ starting with time step 1. This MOT procedure requires $O(N_s^2)$ matrix-fill operations to calculate the integrals in (3.4),

$O(N_s^2)$ memory space to store the matrices, and $O(N_t N_s^2)$ operations for time marching [18].

3.2 Temporal Basis Functions

Two classes of interpolatory temporal basis functions are commonly used for constructing the matrices in (3.4): CPPIFs [5, 17-19] and BLIFs [20-22]. On the one hand, CPPIFs automatically satisfy the march criterion because they are discretely causal; i.e., the Q^{th} order CPPIF is non-zero only for $-\Delta t < t < Q\Delta t$. The CPPIFs are constructed by using polynomial interpolation in backward-looking (causal) sub-domains [Fig. 3.1(a)]; they are expressed in Lagrange form as

$$\text{Lgrg}^{Q}(t) = \begin{cases} \prod_{j=-Q+q, j\neq 0}^{q} \dfrac{t - j\Delta t}{j\Delta t} & (q-1)\Delta t \le t \le q\Delta t \\ 0 & \text{otherwise} \end{cases} \tag{3.6}$$

for $q \in \{0,..,Q\}$. On the other hand, BLIFs do not satisfy the march criterion; indeed, they are even functions, e.g., let prol^{M} denote the BLIF with a width parameter M, then its non-zero for $|t| < M\Delta t$ [Fig. 3.1(b)]. The BLIFs are constructed by truncating an approximation to the prolate spheroidal wave function that is essentially zero for $|t| \ge M\Delta t$ [28]; they are expressed as

$$\text{prol}^{M}(t) = \begin{cases} \text{sinc}\left(\dfrac{\pi f_{\max} t}{\beta}\right) \dfrac{\text{sinc}\left(a\sqrt{\left(t/M\Delta t\right)^2 - 1}\right)}{a\sinh(a)} & |t| < M\Delta t \\ 0 & \text{otherwise} \end{cases} \tag{3.7}$$

Here, $a = \pi M(1-2\beta)$ is a measure of the time-bandwidth product of the BLIFs. Despite their lack of causality, an MOT solution can be recovered for BLIFs by employing a band-limited extrapolation scheme at each time step to approximate the $M-1$ future current coefficients in terms of the present and past ones [20], i.e., at time step l, the coefficients $\mathbf{I}_{l+1},...,\mathbf{I}_{l+M-1}$ are approximated using the N_{samp} coefficients $\mathbf{I}_{l-N_{samp}+1},...,\mathbf{I}_{l}$

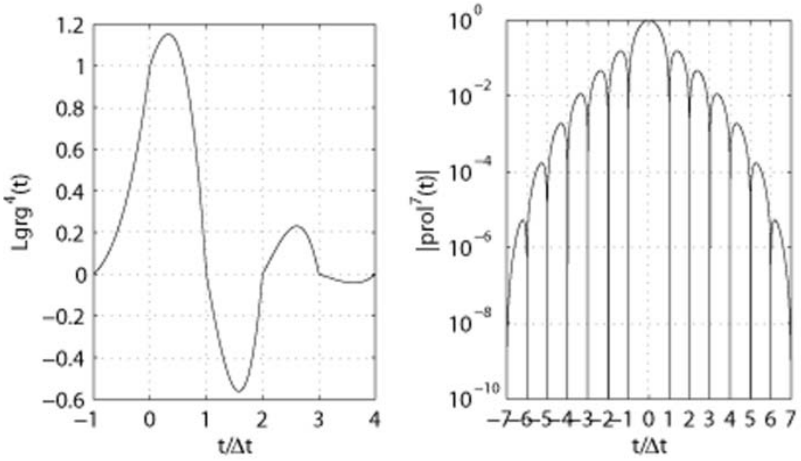

(a) (b)

Figure 3.1: Temporal basis functions: (a) $Q = 4$ CPPIF and (b) $M = 7$ BLIF.

as

$$\mathbf{I}_{l+m}^{\mathrm{X}} = \sum_{m'=1-N_{\mathrm{samp}}}^{0} h_{m,m'} \mathbf{I}_{l+m'} \text{ for } m = 1,\ldots,M-1 \tag{3.8}$$

where $h_{m,m'}$ is the extrapolation coefficient that relates $\mathbf{I}_{l+m'}$ to $\mathbf{I}_{l+m}^{\mathrm{X}}$, the approximation of $\mathbf{I}_{l+m}$ [20].

3.3 Error Sources

There are several sources of error in the numerical solution of (2.1) that are directly affected by the choice of the temporal basis function. These include the errors made in interpolation, integration, and when BLIFs are used, extrapolation.

3.3.1 Interpolation Errors

Interpolation errors are incurred when the temporal variation of the current density is approximated from its samples as in (2.2); the interpolation error for each $\mathbf{S}_{k'}$ is given as $|J_{k'}(t) - \sum_{l'=1}^{N_t} I_{k',l'} T_{l'}(t)|$ at all times t. Because $J_{k'}$ are band-limited finite-energy signals, this error can be reduced by either (i) increasing the order/length of the

basis function or (ii) reducing the time step size/increasing the sampling rate. Indeed, for such signals, the error convergence is of polynomial and exponential order with the length of CPPIFs and BLIFs, respectively, i.e., the interpolation error is bounded by $C_1 B(2\pi\beta)^{Q+1}$ for $\mathrm{Lgrg}^Q(t)$ [29] and by $C_2 / \sinh(\pi M(1-2\beta))$ for $\mathrm{prol}^M(t)$ [28], where C_1 and C_2 are constants and B^2 is the total energy of $J_{k'}$. These convergence properties are demonstrated next by interpolating a common waveform, a cosine modulated Gaussian pulse

$$G(t) = \cos(2\pi f_c t)\, \mathrm{e}^{-0.5\left((t-t_d)/\sigma\right)^2} \tag{3.9}$$

Here, σ is the standard deviation, f_c is the center frequency, and t_d is the center of the pulse. The errors are compared using the L2 norm

$$\mathrm{err}_l^{\mathrm{I}} = \sqrt{\int_{(l-1)\Delta t}^{l\Delta t} \left(G(t) - \sum_{l'=l-t_e}^{l+t_s+1} G(l'\Delta t) T_{l'}(t) \right)^2 dt \Bigg/ \int_{(l-1)\Delta t}^{l\Delta t} G^2(t)\, dt} \tag{3.10}$$

which quantifies the relative interpolation error at the time interval $(l-1)\Delta t \le t \le l\Delta t$. Fig. 3.2 shows the maximum of this error among all time intervals in the range $0 \le l \le \lceil 0.1\mu\mathrm{s} / \Delta t \rceil$ for various basis functions as the time step size is reduced from $\Delta t = 5$ ns ($\beta = 0.5$) to $\Delta t = 0.125$ ns ($\beta = 0.0125$). Here, the pulse parameters are set to $f_c = 300$ MHz, $\sigma = 3/(2\pi f_{bw})$, $f_{bw} = 100$ MHz, and $t_d = 8\sigma$. As expected, CPPIFs and BLIFs exhibit polynomial and exponential convergence with respect to their lengths and their errors converge to zero and to constant values as Δt decreases to zero, respectively. Notice the significantly lower levels of error for BLIFs for $0.05 \le \beta \le 0.1$, which is a typical range of time step sizes used in MOT analysis [17, 19, 22]. It is important to note that the first and second derivatives of the current density are also used in (2.1). Because these are interpolated using the derivatives of the temporal basis function as shown in (3.4), their interpolation errors converge slower, e.g., the interpolation error for the second temporal derivative is bounded by $C_3 B(2\pi\beta)^{Q-1}$ for $\mathrm{Lgrg}^Q(t)$ and by

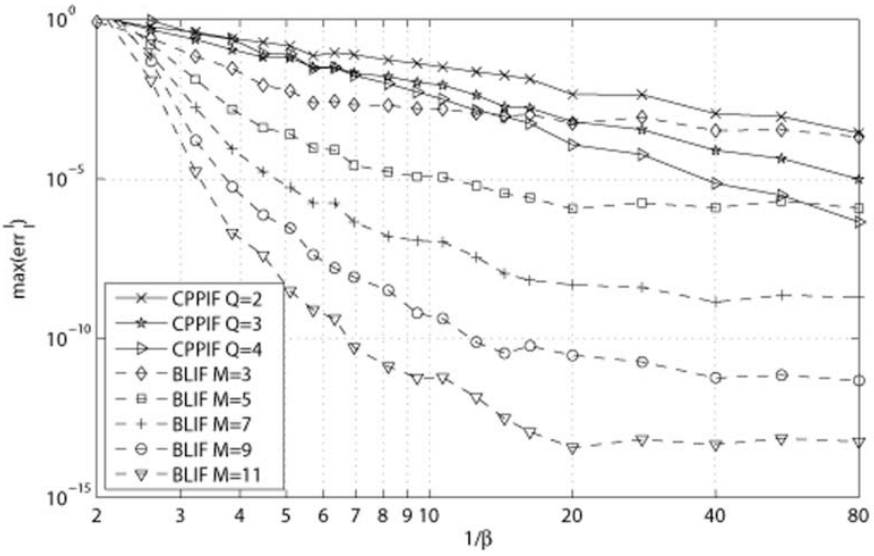

Figure 3.2: The maximum interpolation error for a modulated Gaussian pulse.

$\left(C_4 + C_5(\Delta t)^{-1} + C_6(\Delta t)^{-2}\right) \Big/ \sinh(\pi M[1-2\beta]$, for $\text{prol}^M(t)$, where C_3, C_4, C_5 and C_6 are constants.

3.3.2 Integration Errors

Although increasing the order/length of the basis functions and decreasing the time step size (down to around $\beta = 0.05$ for BLIFs [Fig. 3.2]) can reduce interpolation errors, both approaches adversely affect the evaluation of the integrals in (3.4).

The first approach is generally a minor source of integration error: Higher order/wider basis functions (and BLIFs compared to CPPIFs) result in more complicated integrands that require higher order cubature rules (and singularity extraction techniques); this complication is relatively inexpensive to combat and marginally increases the matrix-fill cost, the memory requirement, and the time-marching cost.

The second approach can be a major source of integration error: As Δt decreases, standard cubature rules defined over the domains of spatial basis/testing functions become ineffective because *all* of the integrands in (3.4) become localized to (are non-

zero in) regions smaller than their integration domains; this implies a lower bound of $\Delta t \sim \Delta r/(Qc_0)$ or $\Delta t \sim \Delta r/(Mc_0)$ for standard cubature rules, where Δr denotes the average linear dimension of spatial domains. The lower bound on Δt is even higher for CPPIFs because they are only piecewise differentiable: Derivatives of CPPIFs contain jump discontinuities at the sampling instances (at multiples of Δt) and thus the vector potential integrands in (3.4) become discontinuous when $\Delta t \le \Delta r/c_0$. In contrast, BLIFs have continuous derivatives everywhere except at the beginning and end of their intervals (at t_s and t_e); thus, discontinuous integrands are not observed in most integration domains until $\Delta t \sim \Delta r/(Mc_0)$. To overcome this problem, special cubature rules must be devised by defining the domains of integration to where the integrands are nonzero; for common spatial basis functions, semi-analytical integration formulas can also be devised [19, 30-32]. These solutions, however, increase the matrix-fill operations significantly and cannot be integrated with fast algorithms that are based on standard cubature rules [17, 18]. Thus, in practice, integration errors limit how small Δt can be: If, as is typical, 10 elements are used per minimum wavelength of interest, then $c_0\Delta t \sim \Delta r$ when $\beta \sim 0.1$, i.e., integration errors become significant when $\Delta t < 0.1/f_\mathrm{max}$ for CPPIFs.

3.3.3 Extrapolation Errors

The march criterion requires that the left-hand-side of (3.3) be calculated in terms of only the present and past current coefficients. To satisfy this criterion, an extrapolation scheme must be used for the non-causal BLIFs; as described in Section 2.2, this implies that at each time step the current coefficients at the following $M-1$ time steps are found approximately. These approximate coefficients, especially those furthest in the future [20], are erroneous and thus corrupt the calculation of the left-hand-side of (3.3). The magnitude of the corruption depends on how well the *past* current density is

approximated (due to the causality of the Green's function). Thus, the extrapolation error at time step l for each $\mathbf{S}_{k'}$ can be quantified as $|J_{k'}(t)-\sum_{l'=1}^{l} I_{k',l'}T_{l'}(t)-\sum_{m=1}^{M-1} I^{\mathrm{X}}_{k',l+m}T_{l+m}(t)|$ for $t \le l\Delta t$; here, the extrapolated current coefficients are given by $I^{\mathrm{X}}_{k',l+m}=\sum_{m'=1-N_{\mathrm{samp}}}^{0} h_{m,m'}I_{k',l+m'}$. Notice that this error expression is identical to the interpolation error defined in Section 2.3.1 for $t \le (l+1-M)\Delta t$; to demonstrate their differences, the cosine modulated Gaussian pulse in Fig. 3.2 is used again and the extrapolation error is quantified using an L2 norm error similar to :

$$\mathrm{err}_l^{\mathrm{X}}=\sqrt{\frac{\int_{(l-1)\Delta t}^{l\Delta t}\left(G(t)-\sum_{l'=l-1-t_{\mathrm{end}}}^{l} G(l'\Delta t)T_{l'}(t)-\sum_{m=1}^{M-1} G^{\mathrm{X}}_{l+m}T_{l+m}(t)\right)^2 dt}{\int_{(l-1)\Delta t}^{l\Delta t} G^2(t)dt}} \tag{3.11}$$

where G^{X}_{l+m} denotes the samples of the pulse extrapolated at time $l\Delta t$. Fig. 3.3 compares the minimum and maximum values of the interpolation error $\mathrm{err}_l^{\mathrm{I}}$ and the extrapolation error $\mathrm{err}_l^{\mathrm{X}}$ among all time intervals in the range $0 \le l \le \lceil 0.1\mu\mathrm{s}/\Delta t \rceil$. The same pulse parameters are used as in Fig. 3.2, N_{samp} is set to 8, and the extrapolation coefficients are found by using the least square scheme of [20] with the parameter $N_\omega = 16$. Figs. 3.3(a)-(d) show the minimum and maximum errors versus the BLIF width parameter for various time step sizes. It can be observed that the minimum (maximum) interpolation errors are identical to the corresponding extrapolation errors until $M=7$ ($M=4$) in all cases, which indicates that the main error source is interpolation rather than extrapolation operations. For larger M, however, extrapolation errors are higher than interpolation errors and stop converging with M, i.e., extrapolation becomes the main limit for the achievable accuracy. Fig. 3.3 also shows that the maximum and minimum $\mathrm{err}_l^{\mathrm{X}}$ decreases with increase in sampling rate; however, the error decreases only up to a certain sampling

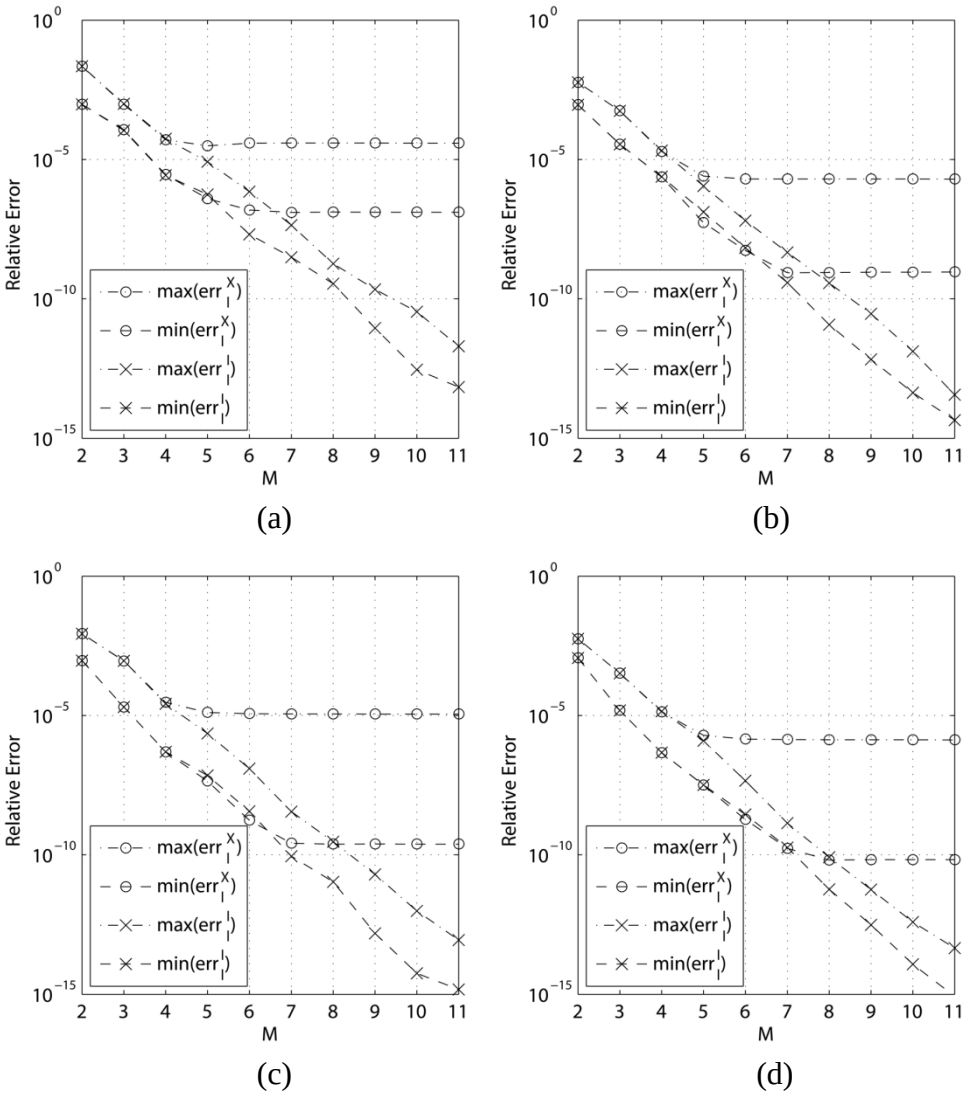

Figure 3.3: Interpolation versus extrapolation errors. The minimum and maximum errors are shown for the same pulse as in Fig. 3.2 when (a) $\beta = 1/10$, (b) $\beta = 1/20$, (c) $\beta = 1/30$, and (d) $\beta = 1/40$.

rate ($\beta = 0.025$ for this example) and cannot be made arbitrarily small. In short, unlike interpolation errors, the extrapolation errors have a non-zero minimum; they can be decreased only down to this minimum level by increasing M or decreasing Δt.

3.4 Numerical Results

In this section, the effects of the temporal basis functions on the accuracy and computational costs of the MOT solution are quantified by solving several scattering problems. The errors are measured by referring to a method-of-moments (MOM) solution, which solves the CFIE in (2.1) in frequency-domain using the same spatial basis/testing functions, and cubature rules as the MOT solution; this guarantees that the difference between the two solutions are purely due to their treatment of the temporal variations. Specifically, the current coefficients found by the MOT solution are Fourier transformed and compared to the current coefficients found by the MOM solution using the norm

$$\mathrm{err}(f)=\sqrt{\frac{\sum_{k'=1}^{N_s}\left(\tilde{J}_{k'}(f)-\tilde{J}_{k'}^{\mathrm{MOM}}(f)\right)^2}{\sum_{k'=1}^{N_s}\left(\tilde{J}_{k'}^{\mathrm{MOM}}(f)\right)^2}} \tag{3.12}$$

Here, $\tilde{J}_{k'}$ denotes the Fourier transform of $J_{k'}$ and $\tilde{J}_{k'}^{\mathrm{MOM}}$ denotes the reference MOM solution. All results in this section are obtained on a parallel cluster of 2.66 GHz Xeon dual-core processors (the wall-clock timing data are scaled to a serial machine assuming ideal scalability); all CFIEs are formulated with $\alpha = 0.5$ and spatially discretized using RWG functions [23]; all extrapolation coefficients for BLIFs are found by using the scheme of [20] with the parameter N_ω set to $2N_{\mathrm{samp}}$; and all scatterers are illuminated with a Gaussian plane wave, i.e., $\mathbf{E}^{\mathrm{inc}}(\mathbf{r},t)=\hat{p}G(t-\hat{r}\cdot\hat{k}_0/c_0)$, where $\hat{p}$ is the wave polarization and $\hat{k}_0$ is the direction of propagation.

3.4.1 Sphere

The first structure is a sphere of radius $1.25\lambda_{\min}$; the surface current density on the sphere is discretized with $N_s = 7431$ RWG functions; and the incident pulse parameters are $f_{\mathrm{c}} = 281.25$ MHz, $f_{\mathrm{bw}} = 93.75$ MHz, $\hat{k}_0 = -\hat{z}$, and $\hat{p} = \hat{z}$. Figs. 3.4(a)-(c) show the error at

$f_{\max} = 375$ MHz versus the MOT matrix-fill time, memory requirement, and marching time for the different temporal functions. The plots are obtained by (i) varying the time step size ($5 \le 1/\beta \le 65$), the Gaussian cubature rule (for orders 5-9), and the extrapolation length ($5 \le N_{\text{samp}} \le 9$), (ii) recording the error and the computational costs, and (iii) choosing the parameters that minimize the time-marching cost at each error level. A single simulation with one set of parameters is used to obtain three data points in the three plots, i.e., the parameters are not varied to minimize different costs. Even smaller time step sizes could not be used because they lead to unstable solutions due to integration errors (see Section 3.3.2).

The following can be observed for CPPIFs: (i) Fig. 3.4(a) shows that the time required for matrix-fill operations is insensitive to the error level, i.e., changing the desired error level (by changing Q or Δt) in the $3\times10^{-4} - 6\times10^{-1}$ range changes the matrix-fill time by less than a factor of 1.5. (ii) Figs. 3.4(b)-(c) show that the error is polynomial in the memory requirement and marching time. (iii) Among CPPIFs, the $Q = 4$ CPPIF requires the least memory, the least time for marching, and the highest matrix fill time (but with a negligible margin) for achieving engineering accuracies, i.e., error levels in the $10^{-3} - 10^{-1}$ range. In contrast, the BLIFs exhibit a more complex accuracy-efficiency tradeoff: The error is not controllable for $M = 3$ (because the interpolation accuracy is insensitive to Δt, see Fig. 3.2); it varies in a narrow range $(10^{-4} - 10^{-3})$ for $M = 5$; and its range is essentially the same for all $M \ge 7$. The following can be observed for the $M \ge 5$ BLIFs: (i) Fig. 3.4(a) shows that the error versus the matrix-fill time plot is a $\urcorner$-shaped curve: The matrix-fill time is highly sensitive to the error level for larger errors (in the $10^{-4} - 10^{-3}$ range) but insensitive to it for smaller errors (in the $10^{-6} - 10^{-4}$ range). (ii) Figs. 3.4(b)-(c) show that the error versus the memory requirement and marching time plots are $\llcorner$-shaped curves, i.e., the memory requirement

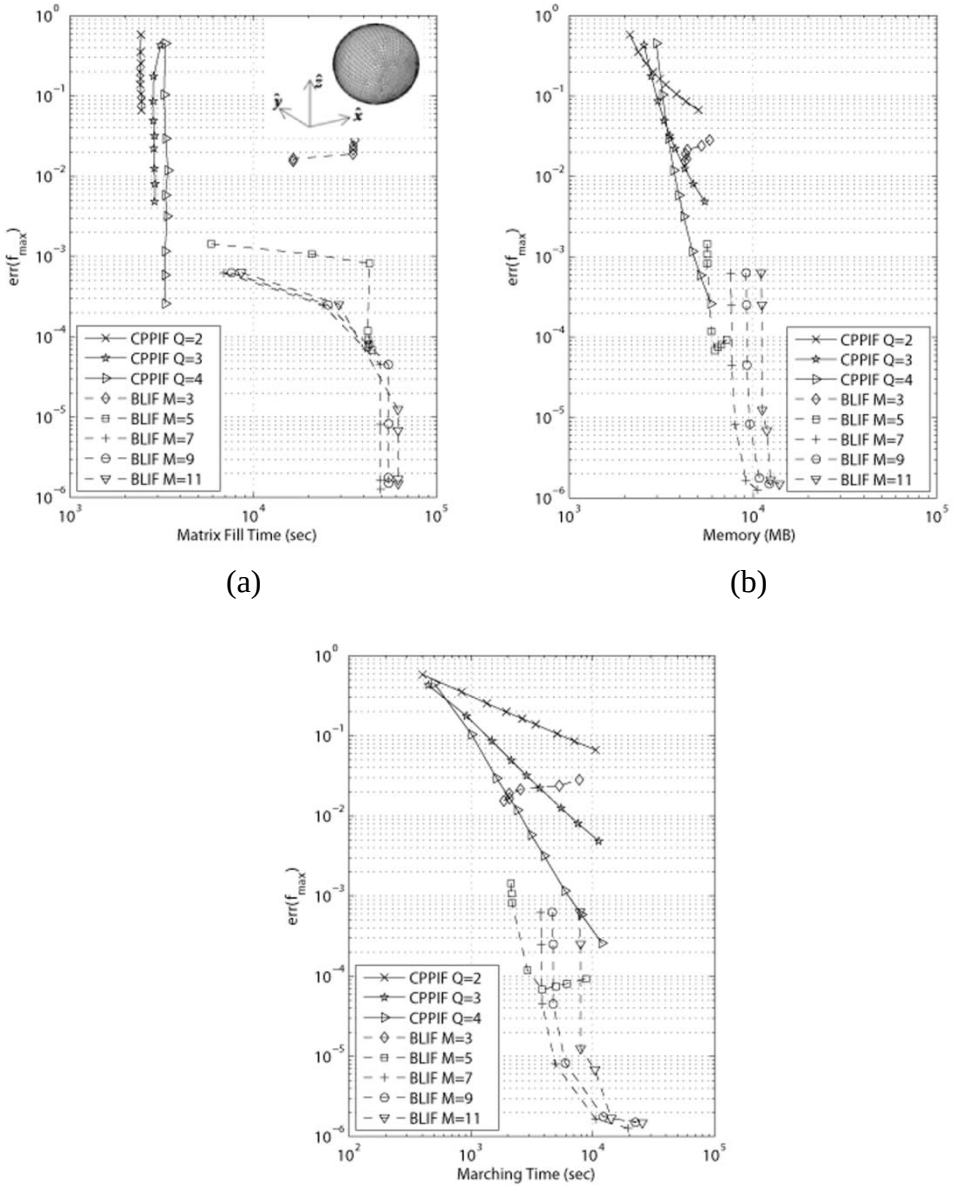

(a) (b)

(c)

Figure 3.4: Accuracy-efficiency tradeoff for a sphere of radius $1.25c_0 / f_{\max}$. The error at the highest frequency is shown versus (a) matrix-fill time, (b) memory requirement, and (c) marching time.

and marching time are insensitive to the error level for larger errors but very sensitive to it for smaller errors. In other words, reducing the error is significantly more costly around

the 10^{-6} level. (iii) All three error vs. cost figures are insensitive to the BLIF width parameter M for $M \geq 7$; indeed, the $M = 7$ BLIF generally requires the least memory, time for marching, and matrix fill time for achieving errors in the $10^{-6} - 10^{-3}$ range. This is expected based on the analysis in Section 3.3.3: When $M \geq 7$, the error is limited by extrapolation accuracy (Fig. 3.3) and thus increasing M only increases the MOT costs and not its accuracy.

Overall, the figures show that it is more efficient to use CPPIFs than BLIFs for error levels down to 10^{-3}; that only BLIFs can achieve errors lower than $\sim 3 \times 10^{-4}$ because CPPIFs are limited by integration errors; and that even BLIFs cannot achieve errors lower than 10^{-6} because they are limited by extrapolation errors.

3.4.2 Almond

To demonstrate that the above observations are valid in general, a NASA almond [26] is discretized using $N_s = 19467$ RWG basis functions. The incident pulse parameters are $f_c = 7$ GHz, $f_{bw} = 2.92$ GHz, $\hat{k}_0 = -\hat{z}$, and $\hat{p} = \hat{z}$. Fig. 3.5(a)-(c) show the error at $f_{max} = 9.92$ GHz versus MOT matrix-fill time, memory requirement, and marching time for the different temporal functions. The plots are obtained just like for the sphere: The time step size ($5 \leq 1/\beta \leq 80$), the Gaussian cubature rule (for orders 5-9), and the extrapolation length ($5 \leq N_{samp} \leq 9$) are varied and the parameters that minimize the time-marching cost are chosen. The efficiency-accuracy characteristics of these results are consistent with the previous structure; e.g., the minimum error achievable by CPPIFs and by BLIFs are again $\sim 10^{-3}$ and $\sim 10^{-6}$, respectively, and the extrapolation limit for BLIFs again is apparent for parameters $M \geq 7$.

3.4.3 Model Aircraft

To further validate the results, another example considered is that of an aircraft model,

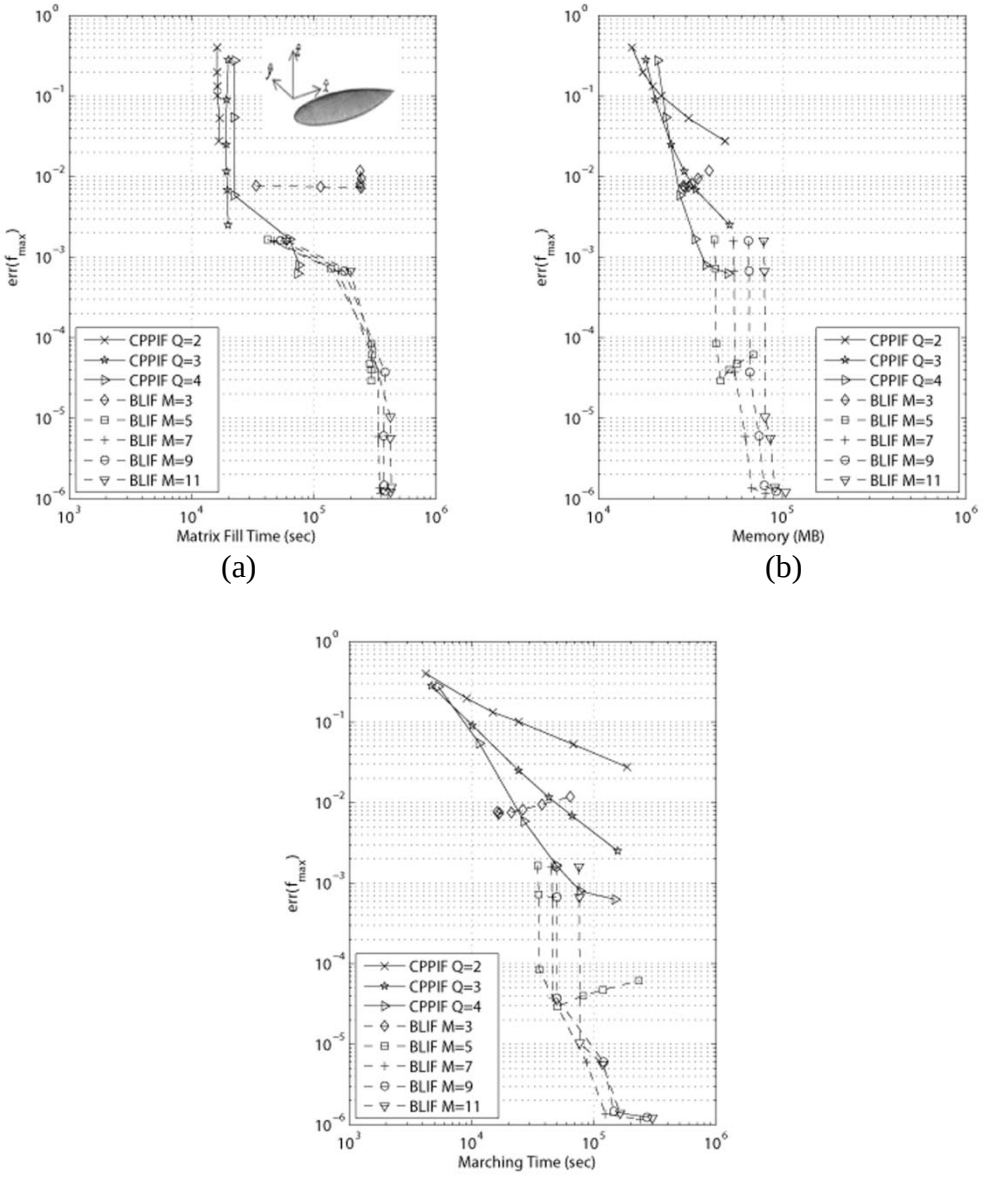

(a) (b)

(c)

Figure 3.5: Accuracy-efficiency tradeoff for the NASA almond. The error at the highest frequency is shown versus (a) matrix-fill time, (b) memory requirement, and (c) marching time.

discretized with $N_s = 16218$ RWG basis functions. The incident pulse parameters are $f_{\max} = 3$ GHz, $f_c = 2$ GHz and $f_{bw} = 1$ GHz, $\hat{\mathbf{k}}_0 = -\hat{\mathbf{y}}$ and $\hat{\mathbf{p}} = \hat{\mathbf{z}}$. Fig. 3.6(a)-(c) show the error at $f_{\max} = 3$ GHz versus MOT matrix-fill time, memory requirement, and marching

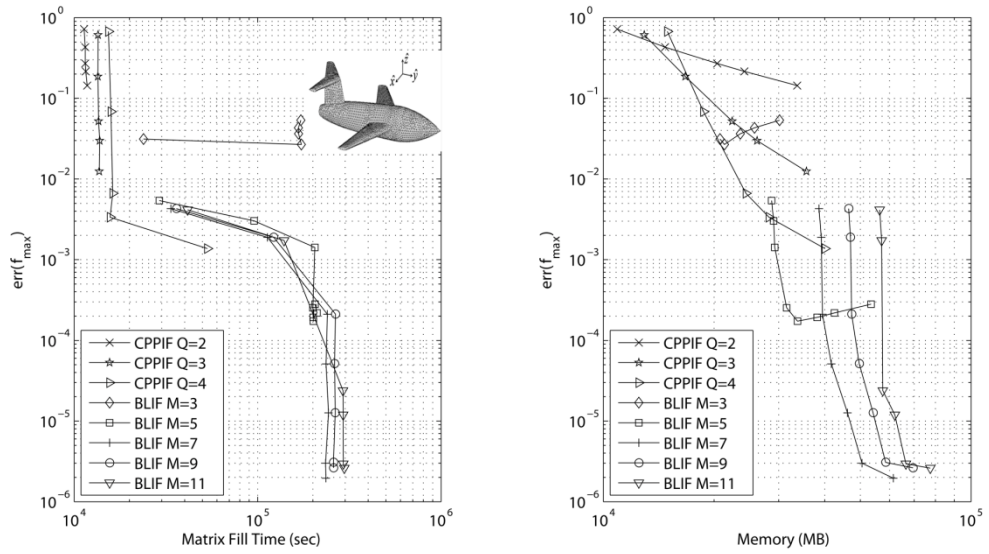

(a)

(b)

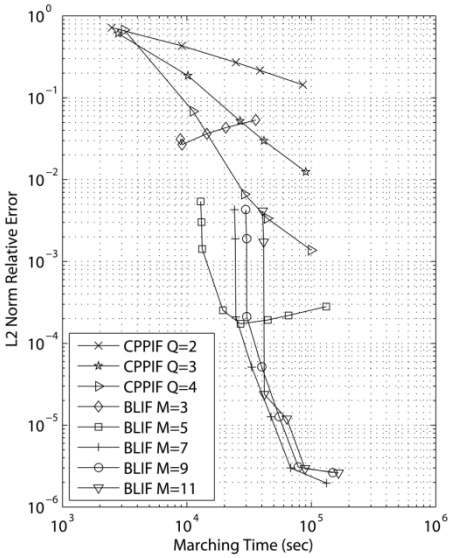

(c)

Figure 3.6: Accuracy-efficiency tradeoff for a model aircraft. The error at the highest frequency is shown versus (a) matrix-fill time, (b) memory requirement, and (c) marching time.

time for the different temporal functions. The performance in terms of efficiency and accuracy observed from these results are consistent with the previous examples.

3.5 Summary

This chapter presented a detailed comparison of two classes of temporal basis functions by studying interpolation, integration, and extrapolation errors for both. The results for the CFIE based MOT solver quantify the efficiency-accuracy tradeoff for a wide range of parameters for CPPIF and BLIF respectively. It is observed that CPPIF is the best choice for low to moderate accuracy levels and that the BLIF is capable of achieving about three orders of magnitude lower errors. It is also observed that the best achievable accuracy from CPPIF is limited by integration errors and that from BLIF is limited by extrapolation errors.

CHAPTER 4: CONCLUSIONS

This thesis presented a detailed study of numerical errors encountered in the solution of frequency- and time-domain integral equations.

In Chapter 2, the two most common approaches for treating singular integrals were presented and their performances were compared. For the SE method, it was observed that the integration accuracy is limited by the number of terms extracted in the asymptotic expansion of the Green's function. For the SC method, a numerical integration technique based on the Gauss-Patterson progressive quadrature rule was developed. Numerical results showed that the SE method is more efficient than the SC method when relative integration errors higher than $\sim 10^{-5}$ are acceptable (e.g., for high-frequency scattering problems solved using low order spatial basis functions). When lower errors are desired, the SE method is preferable if additional terms can be extracted from the integrals and evaluated analytically [12]. The SC method is a preferable choice when closed form integrals needed for the SE method are not available; e.g, when complex Green's functions and high order basis functions are used.

In Chapter 3, a detailed comparison of two classes of temporal basis functions demonstrated the accuracy-efficiency tradeoff when choosing sub-domain temporal basis functions for MOT solvers. The effects of interpolation, integration, and extrapolation errors on the accuracy of MOT solvers were identified theoretically and demonstrated numerically. The results for the CFIE showed that the $Q = 4$ CPPIF is the best choice for engineering accuracies and that the $M = 7$ BLIF can achieve about three orders of magnitude lower errors. It was observed that the minimum errors that can be achieved by both classes of functions are bounded for different reasons: Integration errors limit CPPIFs and extrapolation errors limit BLIFs.

REFERENCES

[1] J. A. Stratton, *Electromagnetic Theory*, New York: McGraw-Hill, 1941.

[2] A. F. Peterson, S. L. Ray, and R. Mittra, *Computational Methods for Electromagnetics*, New York: IEEE Press, 1998.

[3] R. S. Elliott, *Antenna Theory and Design*, Englewood Cliffs, New Jersey: Prentice-Hall, Inc., 1981.

[4] R. F. Harrington, *Field Computation by Moment Methods*, Piscataway, NJ: IEEE Press, 1993.

[5] G. Manara, A. Monorchio, and R. Reggiannini, "A space-time discretization criterion for a stable time-marching solution of the electric field integral equation," *IEEE Trans. Antennas Propagat*., vol. 45, pp. 527–532, 1997.

[6] R. D. Graglia, "The use of parametric elements in the moment method solution of static and dynamic volume integral equations," *IEEE Trans. Antennas Propagat.*, vol. 36, no. 5, pp. 636–646, May 1988.

[7] B. M. Notaros, "Higher order frequency-domain computational electromagnetics," *IEEE Trans. Antennas Propagat.*, vol. 56, no. 8, pp. 2251–2276, Aug. 2008.

[8] M. F. Wu, G. Kaur, and A. E. Yılmaz, "A multiple-grid adaptive integral method for multi-region problems," *IEEE Trans. Antennas Propagat*., vol. 58, no. 5, pp. 1601-1613, May 2010.

[9] D. Wilton, S. Rao, A. Glisson, D. Schaubert, O. Al-Bundak, and C. Butler, "Potential integrals for uniform and linear source distributions on polygonal and polyhedral domains," *IEEE Trans. Antennas Propagat.*, vol. 32, no. 3, pp. 276-281, Mar. 1984.

[10] R. D. Graglia, "On the numerical integration of the linear shape functions times the 3-D Green's function or its gradient on a plane triangle," *IEEE Trans. Antennas Propagat.*, vol. 41, no. 10, pp. 1448-1455, Oct. 1993.

[11] T. F. Eibert and V. Hansen, "On the calculation of potential integrals for linear source distributions on triangular domains," *IEEE Trans. Antennas Propagat.*, vol. 43, no. 12, pp.1499-1502, Dec. 1995.

[12] Y.-O. Pasi and M. Taskinen, "Calculation of CFIE impedance matrix elements with RWG and nxRWG functions," *IEEE Trans. Antennas Propag.*, vol. 51, no. 8, pp. 1837–1846, Aug. 2003.

[13] M. G. Duffy, "Quadrature over a pyramid or cube of integrands with a singularity at a vertex," *SIAM J. Numer. Anal.*, vol. 19, no. 6, pp. 1260–1262, Dec. 1982.

[14] M. A. Khayat and D. R. Wilton, "Numerical evaluation of singular and near-singular potential integrals," *IEEE Trans. Antennas Propagat.*, vol. 53, no. 10, pp. 3180–3190, Oct. 2005.

[15] M. A. Khayat, D. R. Wilton, and P. W. Fink, "An improved transformation and optimized sampling scheme for the numerical evaluation of singular and near-

singular potentials," *IEEE Antennas Wireless Propagat. Lett.*, vol. 7, pp. 377-380, July 2008.

[16] Ismatullah and T. F. Eibert, "Adaptive singularity cancellation for efficient treatment of near-singular and near-hypersingular integrals in surface integral equation formulations," *IEEE Trans. Antennas Propagat*., vol. 56, no. 1, pp. 274-278, Jan. 2008.

[17] B. Shanker, A. A. Ergin, M. Lu, and E. Michielssen, "Fast analysis of transient electromagnetic scattering phenomena using the multilevel plane wave time domain algorithm," *IEEE Trans. Antennas Propagat.*, vol. 51, no. 3, pp. 628-641, Mar. 2003.

[18] A. E. Yılmaz, J. M. Jin, and E. Michielssen, "Time domain adaptive integral method for surface integral equations," *IEEE Trans. Antennas Propagat*., vol. 52, no. 10, pp. 2692-2708, Oct. 2004.

[19] B. Shanker, M. Lu, J. Yuan, and E. Michielssen, "Time domain integral equation analysis of scattering from composite bodies via exact evaluation of radiation fields," *IEEE Trans. Antennas Propag*., vol.57, no.5, pp.1506-1520, May 2009.

[20] D. S. Weile, G. Pisharody, N.-W. Chen, B. Shanker, and E. Michielssen, "A novel scheme for the solution of the time-domain integral equations of electromagnetics," *IEEE Trans. Antennas Propagat*., vol.52, no.1, pp. 283-295, Jan. 2004.

[21] E. Bleszynski, M. Bleszynski, and T. Jaroszewicz, "Fast time domain integral equation solver for dispersive media with auxiliary Green functions," in *Proc. IEEE/ACES Int. Conf. Wirelesss Comm. Appl. Comp. Electromagn.*, pp. 711-718, Apr. 2005.

[22] A. E. Yilmaz, J. M. Jin, and E. Michielssen, "A leapfrogging-in-time integral equation solver," *IEEE Antennas Wireless Propagat. Lett*., pp. 203-206, 2007.

[23] S. M. Rao, D. R. Wilton, and A. W. Glisson, "Electromagnetic scattering by surfaces of arbitrary shape," *IEEE Trans. Antennas Propag.*, vol. AP-30, pp. 409–418, May 1982.

[24] D. J. Taylor, "Accurate and efficient numerical integration of weakly singular integrals in Galerkin EFIE solutions," *IEEE Trans. Antennas Propagat.*, vol.51, no.7, pp. 1630- 1637, July 2003.

[25] M. T. Heath, *Scientific Computing. An Introductory Survey.* McGraw-Hill, Boston, MA, second edition, 2002.

[26] A.C. Woo, H.T.G. Wang, M.J. Schuh, and M.L. Sanders, "EM programmer's notebook-benchmark radar targets for the validation of computational electromagnetics programs," *IEEE Antennas Propagat. Mag.*, vol.35, no.1, pp.84-89, Feb 1993.

[27] B. Shanker, A. A. Ergin, K. Aygün, and E. Michielssen, "Analysis of transient electromagnetic scattering from closed surfaces using a combined field integral equation," *IEEE Trans. Antennas Propagat*., vol. 48, no. 7, pp. 1064–1074, 2000.

[28] J. Knab, "Interpolation of band-limited functions using the approximate prolate series," *IEEE Trans. Inform. Theory*, vol.25, no.6, pp. 717- 720, Nov 1979.

[29] R. Radzyner and P. Bason, “An error bound for Lagrange interpolation of low-pass functions,” *IEEE Trans. Inform. Theory*, vol.18, no.5, pp. 669- 671, Sep 1972.

[30] J. Pingenot, S. Chakraborty, and V. Jandhyala, “Polar integration for exact space-time quadrature in time-domain integral equations,” *IEEE Trans. Antennas Propagat*., vol. 54, pp. 3037–3042, 2006.

[31] Y. Shi, M. Y. Xia, R. S. Chen, E. Michielssen, and M. Lu, “A stable marching-in-on-time solver for time domain surface electric field integral equations based on exact integration technique,” in *Proc. Antennas Propagat. Soc. Int. Symp.*, July 2010.

[32] A. C. Yucel and A. A. Ergin, “Exact evaluation of retarded-time potential integrals for the RWG bases,” *IEEE Trans. Antennas Propag*., vol. 54, no. 5, pp. 1496-1502, May 2006.

[33] M. M. Botha and T. Rylander, “Error analysis of singularity cancellation quadrature on curvilinear triangles,” *International Conference on Electromagnetics in Advanced Application (ICEAA) 2007*., vol., no., pp.810-813, 17-21 Sept. 2007.

[34] R. W. Freund, “A transpose-free quasi-minimal residual algorithm for non-hermitian linear systems,” *SIAM J. Sci. Comput.*, 14, pp. 470-482, 1993.

[35] J. Zhao and W. C. Chew, “Integral equation solution of Maxwell's equations from zero frequency to microwave frequencies,” *IEEE Trans. Antennas Propag*., vol.48, no.10, pp.1635-1645, Oct 2000.

VITAE

Guneet Kaur was born in Jalandhar, India, in 1986. She received the B.S. degree in electrical engineering from Indian Institute of Technology, Roorkee, India, in 2008. She is now a graduate student in Department of Electrical and Computer Engineering in University of Texas at Austin, where she is currently pursuing the Ph.D degree.

Current address: 1624 West 6th Street, Apt A, Austin.

This thesis was typed by Guneet Kaur.